Published for SISSA by Springer

Received: *August 23, 2017*
Revised: *January 15, 2018*
Accepted: *March 8, 2018*
Published: *March 30, 2018*

Migdal effect in dark matter direct detection experiments

Masahiro Ibe,[a,b] **Wakutaka Nakano,**[a] **Yutaro Shoji**[a] **and Kazumine Suzuki**[a]

[a] *ICRR, The University of Tokyo, Kashiwa, Chiba 277-8582, Japan*
[b] *Kavli IPMU (WPI), UTIAS, The University of Tokyo, Kashiwa, Chiba 277-8583, Japan*

E-mail: ibe@icrr.u-tokyo.ac.jp, m156077@icrr.u-tokyo.ac.jp, yshoji@icrr.u-tokyo.ac.jp, ksuzuki@icrr.u-tokyo.ac.jp

Abstract: The elastic scattering of an atomic nucleus plays a central role in dark matter direct detection experiments. In those experiments, it is usually assumed that the atomic electrons around the nucleus of the target material immediately follow the motion of the recoil nucleus. In reality, however, it takes some time for the electrons to catch up, which results in ionization and excitation of the atoms. In previous studies, those effects are taken into account by using the so-called Migdal's approach, in which the final state ionization/excitation are treated separately from the nuclear recoil. In this paper, we reformulate the Migdal's approach so that the "atomic recoil" cross section is obtained coherently, where we make transparent the energy-momentum conservation and the probability conservation. We show that the final state ionization/excitation can enhance the detectability of rather light dark matter in the GeV mass range via the *nuclear* scattering. We also discuss the coherent neutrino-nucleus scattering, where the same effects are expected.

Keywords: Beyond Standard Model, Dark matter, Dark Matter and Double Beta Decay (experiments), Electroweak interaction

ArXiv ePrint: 1707.07258

https://doi.org/10.1007/JHEP03(2018)194

Contents

JHEP03(2018)194

1 Introdcution

The existence of dark matter is overwhelmingly supported by numerous cosmological and astrophysical observations on a wide range of scales. However, the nature of dark matter has not been revealed for almost a century except for its gravitational interactions. The identification of the nature of dark matter is one of the most important challenges of modern particle physics (see [1–3] for review).

Among various candidates for dark matter, the weakly interacting massive particles (WIMPs) are the most extensively studied category of dark matter. The WIMPs couple to the standard model particles via interactions similar in strength to the weak nuclear force. Through the weak interaction, the WIMPs are thermally produced in the early universe, and the relic density is set as they freeze out from the thermal bath [4]. The WIMPs are particularly attractive since the dark matter density does not depend on the details of the initial condition of the universe. The WIMPs are also highly motivated as they are interrelated to physics beyond the standard model such as supersymmetry (see e.g. [5]).

The ambient WIMPs can be directly detected by searching for its scattering with the atomic nuclei [6]. Given a circular speed at around the Sun of $239 \pm 5\,\mathrm{km/s}$ [7], the WIMPs recoil the nuclei elastically with a typical momentum transfer of $q_A \sim 100\,\mathrm{MeV}$ for the target nucleus mass of $m_N \sim 100\,\mathrm{GeV}$.[1] The recoil signatures are detected through ionization, scintillation, and the production of heat in the detectors (see [8–10] for review). To date, for example, liquid xenon detectors such as LUX [11], PandaX-II [12], and XENON1T [13] have put stringent exclusion limits on the spin-independent WIMP-nucleon recoil cross section.

In those experiments, it is usually assumed that the atomic electrons around the recoil nucleus immediately follow the motion of the nucleus. However, it takes some time for the electrons to catch up, which causes ionization and excitation of the recoil atom. The ionization and the excitation result in extra electronic energy injections into the detectors.[2] The importance of such effects on direct detection experiments has been pointed out [14–18]. (See also refs. [19, 20], which discuss the ionization effects in the direct detection experiments for dark matter electron scattering.)

In previous studies, such effects are estimated by using the so-called Migdal's approach [21, 22] (see also [23]). Following [18], we call these effects the Migdal effects. In the Migdal's approach, a state of the electron cloud just after a nuclear recoil is approximated by

$$|\Phi'_{ec}\rangle = e^{-im_e \sum_i \mathbf{v}\cdot\hat{\mathbf{x}}_i} |\Phi_{ec}\rangle\,, \tag{1.1}$$

in the rest frame of the nucleus. Here m_e is the electron mass, $\hat{\mathbf{x}}_i$ the position operator of the i-th electron, $\mathbf{v}$ the nucleus velocity after the recoil, and $|\Phi_{ec}\rangle$ the state of the electron cloud before the nuclear recoil. The probability of ionization/excitation is then given by

$$\mathcal{P} = |\langle \Phi^*_{ec} | \Phi'_{ec} \rangle|^2\,, \tag{1.2}$$

where $|\Phi^*_{ec}\rangle$ denotes either the ionized or excited energy eigenstate of the electron cloud.

In the above analysis, the final state ionization/excitation are treated separately from the nuclear recoil. Thus, the energy-momentum conservation and the probability conservation are made somewhat obscure. In this paper, we reformulate the Migdal effect so that the "atomic recoil" cross section is obtained coherently. In our reformulation, the energy-momentum conservation and the probability conservation are manifest while the final state

[1] For a lighter WIMP than m_N, q_A is suppressed by the reduced mass between the nucleus and the WIMP.

[2] The rates of the ionization/excitation are much smaller than $\mathcal{O}(1)$. Besides, the same effects are expected in the nuclear recoil by neutron injections. Accordingly, those effects are almost always taken into account in detector calibration by the neutron sources automatically.

JHEP03(2018)194

ionization/excitation are treated automatically. We also provide numerical estimates of the ionization/excitation probabilities for isolated atoms of Ar, Xe, Ge, Na, and I.

The Migdal effect should be distinguished from the ionization and the excitation in scintillation processes. The Migdal effect takes place even for a scattering of an isolated atom, while the latter occurs due to the interaction between atoms in the detectors. It should be also emphasized that the Migdal effect can ionize/excite electrons in inner orbitals, which are not expected in scintillation processes. As we will see, the ionization/excitation from the inner orbitals result in extra electronic energy injections in the keV range, which can enhance detectability of rather light dark matter in the GeV mass range.

The organization of the paper is as follows. In section 2, we discuss approximate energy eigenstates of an atomic state by paying particular attention to the total atomic motion. In section 3, we reformulate the atomic recoil cross section with the Migdal effect by taking the energy eigenstates in section 2 as asymptotic states. In section 4, we calculate the Migdal effect with single electron wave functions. In section 5, we estimate the probabilities of the ionization/excitation at a nuclear recoil. In section 6, we discuss implications for dark matter direct detection. In section 7, we briefly discuss the Migdal effect in a coherent neutrino-nucleus scattering. The final section is devoted to our conclusions and discussion.

2 Energy eigenstates of atomic system

As we will see in the next section, the plane wave function of a whole atomic system plays a central role to obtain the nuclear scattering cross section with the Migdal effect. In the following, we consider an isolated neutral atom consisting of a nucleus and N_e electrons. The electrons are not necessarily bounded by the Coulomb potential of the nucleus, and hence, the energy eigenstates can be ionic states with unbouded electrons.

As typical nuclear recoil energy is smaller than $\mathcal{O}(100)\,\mathrm{keV}$, the Hamiltonian of the system is well approximated by the non-relativistic one,

$$\hat{H}_A \simeq \frac{\hat{\mathbf{p}}_N^2}{2m_N} + \hat{H}_{ec}(\hat{\mathbf{x}}_N) = \frac{\hat{\mathbf{p}}_N^2}{2m_N} + \sum_i^{N_e} \frac{\hat{\mathbf{p}}_i^2}{2m_e} + V(\hat{\mathbf{x}}_i - \hat{\mathbf{x}}_N)\,. \tag{2.1}$$

Here, $\hat{\mathbf{p}}_N$ and $\hat{\mathbf{x}}_N$ denote the momentum and the position operators of the nucleus with mass m_N, respectively. The momentum and the position operators of the i-th electron are given by $\hat{\mathbf{p}}_i$ and $\hat{\mathbf{x}}_i$, respectively. The Hamiltonian of the electron cloud, $\hat{H}_{ec}$, depends on the position operator of the nucleus, $\hat{\mathbf{x}}_N$, through the interaction potential $\hat{V}(\hat{\mathbf{x}}_i - \hat{\mathbf{x}}_N)$ ($i = 1 \cdots N_e$). The interaction potential also includes the interactions between the electrons. In the coordinate representation, the energy eigen-equation is reduced to

$$\left(\frac{\hat{\mathbf{p}}_N^2}{2m_N} + \hat{H}_{ec}(\mathbf{x}_N) \right) \Psi_E(\mathbf{x}_N, \{\mathbf{x}\}) = E_A\, \Psi_E(\mathbf{x}_N, \{\mathbf{x}\})\,, \tag{2.2}$$

where the positions (including spinor indices) of the N_e electrons are represented by $\{\mathbf{x}\}$ collectively.

JHEP03(2018)194

2.1 Energy eigenstates of an atom at rest

To solve eq. (2.2), let us first consider the eigenstates of $\hat{H}_{ec}(\mathbf{x}_N)$ for a given $\mathbf{x}_N$,

$$\hat{H}_{ec}(\mathbf{x}_N)\Phi_{ec}(\{\mathbf{x}\}|\mathbf{x}_N) = E_{ec}(\mathbf{x}_N)\Phi_{ec}(\{\mathbf{x}\}|\mathbf{x}_N)\,. \tag{2.3}$$

Since the system is invariant under spatial translations, the energy eigenvalues do not depend on $\mathbf{x}_N$ while the wave functions depend on $\mathbf{x}_N$ only through $\{\mathbf{x}_i - \mathbf{x}_N\}$;

$$E_{ec}(\mathbf{x}_N) = E_{ec}\,, \tag{2.4}$$

$$\Phi_{E_{ec}}(\{\mathbf{x}\}|\mathbf{x}_N) \;= \Phi_{E_{ec}}(\{\mathbf{x}-\mathbf{x}_N\})\,. \tag{2.5}$$

The eigenstates, $\Phi_{E_{ec}}(\{\mathbf{x}-\mathbf{x}_N\})$, provide a complete orthogonal basis of the electron cloud for a given $\mathbf{x}_N$.

Next, let us show that $\Phi_{E_{ec}}$ well approximates an energy eigenfunction of the whole atomic system at rest, i.e.,

$$\Psi^{(\mathrm{rest})}_{E_A}(\mathbf{x}_N, \{\mathbf{x}\}) \equiv \Phi_{E_{ec}}(\{\mathbf{x}-\mathbf{x}_N\})\,. \tag{2.6}$$

By substituting $\Psi^{(\mathrm{rest})}_{E_A}$ to eq. (2.2), the energy eigen-equation results in

$$\frac{\hat{\mathbf{p}}_N^2}{2m_N}\Psi^{(\mathrm{rest})}_{E_A}(\mathbf{x}_N, \{\mathbf{x}\}) = (E_A - E_{ec})\Psi^{(\mathrm{rest})}_{E_A}(\mathbf{x}_N, \{\mathbf{x}\})\,. \tag{2.7}$$

Now, $\Psi^{(\mathrm{rest})}_{E_A}$ (i.e. $\Phi_{E_{ec}}$) depends on $\mathbf{x}_N$ only through $\{\mathbf{x}-\mathbf{x}_N\}$, the momentum of the nucleus is balanced with the electron momentum,

$$\hat{\mathbf{p}}_N\Psi^{(\mathrm{rest})}_{E_A}(\mathbf{x}_N, \{\mathbf{x}\}) = -\sum_i^{N_e}\hat{\mathbf{p}}_i\,\Psi^{(\mathrm{rest})}_{E_A}(\mathbf{x}_N, \{\mathbf{x}\})\,. \tag{2.8}$$

Thus, the left-hand side of eq. (2.7) is expected to be highly suppressed, i.e.,

$$\left\langle \frac{\hat{\mathbf{p}}_N^2}{2m_N} \right\rangle \sim \frac{m_e}{m_N} \times E_{ec}\,, \tag{2.9}$$

for $\Psi^{(\mathrm{rest})}_{E_A}$. Here, we used the fact that the expectation value of the electron kinetic energy is roughly given by

$$\left\langle \frac{\hat{\mathbf{p}}_i^2}{2m_e} \right\rangle \sim \frac{E_{ec}}{N_e}\,. \tag{2.10}$$

Therefore, we find that $\Psi^{(\mathrm{rest})}_{E_A}$ provides an approximate energy eigenstate of the whole atomic system with $E_A \simeq E_{ec}$;

$$\hat{H}_A\Psi^{(\mathrm{rest})}_{E_A}(\mathbf{x}_N, \{\mathbf{x}\}) \simeq E_{ec}\Psi^{(\mathrm{rest})}_{E_A}(\mathbf{x}_N, \{\mathbf{x}\})\,. \tag{2.11}$$

It should be noted that this is nothing but the Born-Oppenheimer approximation.[3]

[3] In passing, eq. (2.8) means that the state $\Psi^{(\mathrm{rest})}_{E_A}$ is also an eigenstate of the total momentum of the atom, i.e.

$$\left(\hat{\mathbf{p}}_N + \sum_{i=1}^{N_e}\hat{\mathbf{p}}_i\right)\Psi^{(\mathrm{rest})}_{E_A}(\mathbf{x}_N, \{\mathbf{x}\}) = 0\,. \tag{2.12}$$

JHEP03(2018)194

2.2 Energy eigenstates of a moving atom

Once we have the energy eigenstates of an atomic system at rest, the energy eigenstates of a moving atom with a velocity $\mathbf{v}$ can be immediately obtained by the Galilei transformation,

$$\Psi_{E_A}(\mathbf{x}_N, \{\mathbf{x}\}) \simeq U(\mathbf{v})\Psi^{(\mathrm{rest})}_{E_A}(\mathbf{x}_N, \{\mathbf{x}\})\,. \tag{2.13}$$

Here the unitary operator of the Galilei transformation is given by

$$U(\mathbf{v}) = \exp\left[im_N\mathbf{v}\cdot\mathbf{x}_N + im_e\sum_{i=1}^{N_e}\mathbf{v}\cdot\mathbf{x}_i\right]\,. \tag{2.14}$$

Under the Galilei transformation, the momentum operators are shifted by

$$U(\mathbf{v})^\dagger\hat{\mathbf{p}}_N U(\mathbf{v}) = \hat{\mathbf{p}}_N + m_N\mathbf{v}\,, \tag{2.15}$$

$$U(\mathbf{v})^\dagger\hat{\mathbf{p}}_i U(\mathbf{v}) = \hat{\mathbf{p}}_i + m_e\mathbf{v}\,, \tag{2.16}$$

and the Hamiltonian is transformed into

$$U(\mathbf{v})^\dagger\hat{H}_A U(\mathbf{v}) = \hat{H}_A + \mathbf{v}\cdot\left(\hat{\mathbf{p}}_N + \sum_{i=1}^{N_e}\hat{\mathbf{p}}_i\right) + \frac{1}{2}\overline{m}_A v^2\,. \tag{2.17}$$

Here we define the nominal mass of the atom by

$$\overline{m}_A = m_N + N_e m_e\,. \tag{2.18}$$

By using eqs. (2.11), (2.8), and (2.17), we find that the boosted wave function Ψ_{E_A} satisfies,

$$\hat{H}_A\Psi_{E_A}(\mathbf{x}_N, \{\mathbf{x}\}) \simeq \left(E_{ec} + \frac{1}{2}\overline{m}_A v^2\right)\Psi_{E_A}(\mathbf{x}_N, \{\mathbf{x}\})\,. \tag{2.19}$$

Therefore, the boosted wave function Ψ_{E_A} provides the approximate energy eigenstate of a moving atom with energy

$$E_A \simeq E_{ec} + \frac{1}{2}\overline{m}_A v^2\,. \tag{2.20}$$

In summary, the eigenstate of the atomic system is approximated by

$$\Psi_{E_A}(\mathbf{x}_N, \{\mathbf{x}\}) \simeq e^{i\mathbf{p}_N\cdot\mathbf{x}_N}e^{i\sum_{i=1}^{N_e}\mathbf{q}_e\cdot\mathbf{x}_i}\Psi^{(\mathrm{rest})}_{E_A}(\mathbf{x}_N, \{\mathbf{x}\})\,, \tag{2.21}$$

$$\mathbf{p}_N = m_N\mathbf{v}\,, \tag{2.22}$$

$$\mathbf{q}_e = m_e\mathbf{v}\,, \tag{2.23}$$

with

$$E_A \simeq E_{ec} + \frac{1}{2}\overline{m}_A v^2\,. \tag{2.24}$$

It should be remembered that $\Psi_{E_A}(\mathbf{x}_N, \{\mathbf{x}\})$ is not an eigenstate of the nucleus momentum $\hat{\mathbf{p}}_N$. Instead, $\Psi_{E_A}(\mathbf{x}_N, \{\mathbf{x}\})$ is an eigenstate of the momentum of the whole atom;

$$\left(\hat{\mathbf{p}}_N + \sum_{i}^{N_e}\hat{\mathbf{p}}_i\right)\Psi_{E_A}(\mathbf{x}_N, \{\mathbf{x}\}) = (\overline{m}_A\mathbf{v})\times\Psi_{E_A}(\mathbf{x}_N, \{\mathbf{x}\})\,. \tag{2.25}$$

Thus, $\mathbf{p}_N$ in eq. (2.21) parametrizes not the nucleus momentum but the eigenvalue of the total momentum $\mathbf{p}_A = \overline{m}_A/m_N \times \mathbf{p}_N = \overline{m}_A\mathbf{v}$. It should be also noted that the energy eigenstate in eq. (2.21) is no more in the realm of the Born-Oppenheimer approximation for $\mathbf{v} \neq 0$ since they are not eigenfunctions of $\hat{H}_{ec}$ for a given $\mathbf{x}_N$.

JHEP03(2018)194

3 Migdal effect: from nuclear recoil to atomic recoil

In this section, we derive the recoil cross section of the atomic system with the final state ionization/excitation.

3.1 Isolated nuclear recoil

Before proceeding further, let us first translate the dark matter-nucleus interaction in field theory to an interaction potential, which will be useful in the later analysis. For now, let us forget the electron cloud and take the nucleus as a free separated particle. In a relativistic field theory, the T-matrix and the invariant amplitude of a scattering process are given by

$$T_{FI} = \langle \mathbf{p}_N^F \mathbf{p}_{DM}^F | \mathbf{p}_N^I \mathbf{p}_{DM}^I \rangle = \mathcal{M} \times i(2\pi)^4 \delta^4(p_N^F + p_{DM}^F - p_N^I - p_{DM}^I) \,. \tag{3.1}$$

Here, the plane waves of the dark matter and the nucleus are normalized by

$$\langle \mathbf{p} | \mathbf{p}' \rangle = (2\pi)^3 2p^0 \delta^3(\mathbf{p}' - \mathbf{p}) \,, \tag{3.2}$$

with p^0 being the relativistic energy of the particle.

As an example, let us consider a contact spin-independent interaction between a Dirac dark matter and nucleons;

$$\mathcal{L} = \sum_{i=p,n} \frac{g_i}{M_*^2} \bar{\psi}_i \psi_i \bar{\psi}_{DM} \psi_{DM} \,, \tag{3.3}$$

where M_* denotes a mass parameter and $g_{p,n}$ are dimensionless coupling constants. In this case, the squared invariant amplitude for the nucleus scattering is given by

$$|\mathcal{M}|^2 = 16 \frac{m_N^2 m_{DM}^2}{M_*^4} \left(g_p Z + g_n (A - Z) \right)^2 \,, \tag{3.4}$$

where Z is the atomic number, A the mass number, and m_{DM} the mass of the dark matter. The corresponding cross section is given by

$$\bar{\sigma}_N \simeq \frac{1}{16\pi} \frac{|\mathcal{M}|^2}{(m_N + m_{DM})^2} \,, \tag{3.5}$$

$$\simeq \frac{1}{\pi} \frac{\mu_N^2}{M_*^4} \left(g_p Z + g_n (A - Z) \right)^2 \,, \tag{3.6}$$

where μ_N is the reduced mass,

$$\mu_N = \frac{m_N m_{DM}}{m_N + m_{DM}} \,. \tag{3.7}$$

In the coordinate representation of quantum mechanics, the above invariant matrix element in eq. (3.1) is reproduced by an interaction potential,

$$\hat{H} = \hat{H}_0 + \hat{V}_{\rm int} \,, \tag{3.8}$$

$$\hat{H}_0 = \frac{\hat{\mathbf{p}}_N^2}{2m_N} + \frac{\hat{\mathbf{p}}_{DM}^2}{2m_{DM}} \,, \tag{3.9}$$

$$\hat{V}_{\rm int} = \frac{-\mathcal{M}}{4 m_N m_{DM}} \delta^3(\mathbf{x}_N - \mathbf{x}_{DM}) \,, \tag{3.10}$$

JHEP03(2018)194

with the initial and the final states

$$\psi_I(\mathbf{x}_N, \mathbf{x}_{DM}) = \sqrt{2m_N}\, e^{i\mathbf{p}_N^I\cdot\mathbf{x}_N} \times \sqrt{2m_{DM}}\, e^{i\mathbf{p}_{DM}^I\cdot\mathbf{x}_{DM}}\,, \tag{3.11}$$

$$\psi_F(\mathbf{x}_N, \mathbf{x}_{DM}) = \sqrt{2m_N}\, e^{i\mathbf{p}_N^F\cdot\mathbf{x}_N} \times \sqrt{2m_{DM}}\, e^{i\mathbf{p}_{DM}^F\cdot\mathbf{x}_{DM}}\,. \tag{3.12}$$

Here, we normalize the initial and the final wavefunctions in conforming with the one in eq. (3.2) with the relativistic energies approximated by their masses.

As another example, we may also consider a dark matter interaction with nucleons through an exchange of a light scalar particle, ϕ, with mass m_ϕ,

$$\mathcal{L} = -\sum_{i=p,n} y_i \phi\, \bar{\psi}_i \psi_i - y_{DM}\phi\, \bar{\psi}_{DM}\psi_{DM}\,, \tag{3.13}$$

where $y_{p,n,DM}$ are Yukawa coupling constants. The invariant amplitude of the isolated nuclear scattering for each spin is given by

$$\mathcal{M}(q_N^2) \simeq y_{DM}\left(y_p Z + y_n(A-Z)\right)\frac{4m_{DM}m_N}{m_\phi^2 - t}\,, \tag{3.14}$$

$$t \simeq -q_N^2 = -(\mathbf{p}_N^F - \mathbf{p}_N^I)^2\,, \tag{3.15}$$

in the non-relativistic limit. In the coordinate representation of quantum mechanics, the invariant amplitude is reproduced by adding a potential term

$$\hat{V}_{\rm int}(\mathbf{x}_N - \mathbf{x}_{DM}) = -\int \frac{d^3\mathbf{q}}{(2\pi)^3} e^{i\mathbf{q}\cdot(\mathbf{x}_N - \mathbf{x}_{DM})}\frac{\mathcal{M}(q^2)}{4m_{DM}m_N}\,, \tag{3.16}$$

with the initial and the final state wave functions in eqs. (3.11) and (3.12).

In both cases, the differential cross section with respect to the nuclear recoil energy in the laboratory frame is given by[4]

$$\frac{d\sigma_N}{dE_R} \simeq \frac{1}{32\pi}\frac{m_N}{\mu_N^2 v_{DM}^2}\frac{|F_A(q_N^2)|^2|\mathcal{M}(q_N^2)|^2}{(m_N + m_{DM})^2} = \frac{1}{2}\frac{m_N}{\mu_N^2 v_{DM}^2}\tilde{\sigma}_N(q_N)\,. \tag{3.18}$$

Here, we introduce the nuclear form factor, which is relevant for a momentum transfer q_N in the tens to hundreds MeV. In the last equality, we defined

$$\tilde{\sigma}_N(q_N) = \frac{1}{16\pi}\frac{|F_A(q_N^2)|^2|\mathcal{M}(q_N^2)|^2}{(m_N + m_{DM})^2}\,, \tag{3.19}$$

which reduces to $|F_A(q_N^2)|^2 \times \bar{\sigma}_N$ for the contact interaction.

[4]The elastic nuclear recoil energy is related to the scattering angle in the center of the mass frame via

$$dE_R = \frac{\mu_N^2}{m_N} v_{DM}^2 \times d\cos\theta_{CM}\,. \tag{3.17}$$

JHEP03(2018)194

3.2 Invariant amplitudes with electron cloud

Now, let us calculate the cross section of the nuclear recoil in the presence of electron cloud. For this purpose, we consider

$$\hat{H}_{\rm tot} = \hat{H}_A + \frac{\hat{\mathbf{p}}_{DM}^2}{2m_{DM}} + \hat{V}_{\rm int}\,, \tag{3.20}$$

in the coordinate representation, where $\hat{H}_A$ is given in eq. (2.1). In subsection 3.1, we considered the asymptotic states consist of the plane waves of dark matter and an isolated nucleus. To take into account the electron cloud, we replace the plane waves of the nucleus with the plane waves of the atomic system discussed in section 2.

The initial and the final states of dark matter scattering are taken to be

$$\Psi_I(\mathbf{x}_N, \{\mathbf{x}\}, \mathbf{x}_{DM}) = \sqrt{2m_N}\Psi_{E_A^I}(\mathbf{x}_N, \{\mathbf{x}\}) \times \sqrt{2m_{DM}} e^{i\mathbf{p}_{DM}^I \cdot \mathbf{x}_{DM}}\,, \tag{3.21}$$

$$\Psi_F(\mathbf{x}_N, \{\mathbf{x}\}, \mathbf{x}_{DM}) = \sqrt{2m_N}\Psi_{E_A^F}(\mathbf{x}_N, \{\mathbf{x}\}) \times \sqrt{2m_{DM}} e^{i\mathbf{p}_{DM}^F \cdot \mathbf{x}_{DM}}\,. \tag{3.22}$$

Hereafter, we consider the initial atom at rest in the laboratory frame, $\mathbf{v}_I = 0$. The total energies of the initial and the final states are given by

$$E_I = E_{ec}^I + \frac{{\mathbf{p}_{DM}^I}^2}{2m_{DM}}\,, \tag{3.23}$$

$$E_F = E_{ec}^F + \frac{\overline{m}_A}{2}{v_F}^2 + \frac{{\mathbf{p}_{DM}^F}^2}{2m_{DM}}\,, \tag{3.24}$$

where $E_{ec}^{I,F}$ are the energy eigenvalues of the initial and the final electron clouds in the rest frame, respectively. By using the energy eigenfunctions in eq. (2.21), the T-matrix of this process is given by

$$\begin{aligned} iT_{FI} &= -i(2\pi)\delta(E_F - E_I) \int d^3\mathbf{x}_N d^3\mathbf{x}_{DM} \prod_i d^3\mathbf{x}_i\, 2m_{DM} 2m_N \hat{V}_{\rm int}(\mathbf{x}_N - \mathbf{x}_{DM}) \\ &\quad \times \Phi^*_{E_{ec}^F}(\{\mathbf{x} - \mathbf{x}_N\}) e^{-i\sum_i \mathbf{q}_e \cdot \mathbf{x}_i} e^{-i\mathbf{p}_N^F \cdot \mathbf{x}_N} \Phi_{E_{ec}^I}(\{\mathbf{x} - \mathbf{x}_N\}) e^{-i(\mathbf{p}_{DM}^F - \mathbf{p}_{DM}^I)\cdot \mathbf{x}_{DM}}\,, \quad (3.25) \\ &= -i(2\pi)^4 \delta(E_F - E_I)\delta^3(\overline{m}_A \mathbf{v}_F + \mathbf{p}_{DM}^F - \mathbf{p}_{DM}^I) F_A(q_A)\mathcal{M}(q_A) \\ &\quad \times \int \prod_i d^3\mathbf{x}_i\, \Phi^*_{E_{ec}^F}(\{\mathbf{x}\}) e^{-i\sum_i \mathbf{q}_e \cdot \mathbf{x}_i} \Phi_{E_{ec}^I}(\{\mathbf{x}\})\,, \quad (3.26) \\ q_A^2 &= (\mathbf{p}_{DM}^F - \mathbf{p}_{DM}^I)^2\,. \quad (3.27) \end{aligned}$$

In the second equality, we shifted the integration variables $\mathbf{x}_i$ and $\mathbf{x}_{DM}$ by $\mathbf{x}_N$.

As a result, we obtain the matrix element

$$iT_{FI} \simeq F_A(q_A^2)\mathcal{M}(q_A^2) \times Z_{FI}(\mathbf{q}_e) \times i(2\pi)^4 \delta^4(p_F - p_I)\,, \tag{3.28}$$

where

$$\delta^4(p_F - p_I) = \delta\left(E_F - E_I\right) \times \delta^3(\overline{m}_A \mathbf{v}_F + \mathbf{p}_{DM}^F - \mathbf{p}_{DM}^I)\,, \tag{3.29}$$

$$Z_{FI}(\mathbf{q}_e) = \int \prod_i d^3\mathbf{x}_i\, \Phi^*_{E_{ec}^F}(\{\mathbf{x}\}) e^{-i\sum_i \mathbf{q}_e \cdot \mathbf{x}_i} \Phi_{E_{ec}^I}(\{\mathbf{x}\})\,, \tag{3.30}$$

$$\mathbf{q}_e = m_e \mathbf{v}_F\,, \tag{3.31}$$

JHEP03(2018)194

for $\mathbf{v}_I = 0$.[5] The term proportional to $\mathcal{M}$ denotes the nuclear recoil while the factor $Z_{FI}(\mathbf{q}_e)$ denotes the transition of the electron cloud. It should be emphasized that our approach treats the nucleus and the electron cloud coherently. This treatment enables us to derive the invariant amplitude with manifest energy-momentum conservation.

3.3 Phase space integration

By noting the normalizations in eqs. (2.21), (3.2), (see also (A.1)), the differential cross section is given by[6]

$$d\sigma \simeq \sum_{E^F_{ec}} \frac{d^3\mathbf{p}^F_A}{(2\pi)^3 2p^{F0}_A} \frac{d^3\mathbf{p}^F_{DM}}{(2\pi)^3 2{p^F_{DM}}^0} \frac{|F_A(q^2_A)|^2 |\mathcal{M}(q^2_A)|^2 \times |Z_{FI}(\mathbf{q}_e)|^2}{4\sqrt{(p^I_A \cdot p^I_{DM})^2 - m^2_A m^2_{DM}}} \times (2\pi)^4 \delta^4(p^F_A + p^F_{DM} - p^I_A - p^I_{DM}) \,. \tag{3.32}$$

Here, we defined the physical mass of the atomic system, m_A by

$$m_A = \overline{m}_A + E_{ec} \,. \tag{3.33}$$

By boosting four momentum $(m_A, 0, 0, 0)$, we obtain the four-momentum of the atomic system in an arbitrary frame. For example, the final state four-momentum is given by

$$p^F_A \simeq (p^{F0}_A, \overline{m}_A \mathbf{v}_F) \,, \quad p^{F0}_A \simeq m^F_A + \frac{1}{2}\overline{m}_A v^2_F = \overline{m}_A + E^F_{ec} + \frac{1}{2}\overline{m}_A v^2_F \,, \tag{3.34}$$

in the laboratory frame.

When the magnetic quantum numbers of the electrons in the initial/final states are averaged/summed, the factor $|Z_{FI}(\mathbf{q}_e)|^2$ depends only on the size of $\mathbf{q}_e$. In this case, the differential cross section is given by

$$\frac{d\sigma}{d\cos\theta_{CM}} \simeq \sum_{E^F_{ec}} \frac{1}{32\pi} \frac{|\mathbf{p}_F|}{(p^I_A{}^0 + {p^I_{DM}}^0)^2 |\mathbf{p}_I|} |F_A(q^2_A)|^2 |\mathcal{M}(q^2_A)|^2 |Z_{FI}(q_e)|^2 \,. \tag{3.35}$$

Here, $\mathbf{p}_{I,F}$ denotes the initial and the final state momenta in the center of the mass frame.

[5] The Fermi's golden rule is justified by taking the timescale much loner than $(E^F_{ec} - E^I_{ec})^{-1}$. This timescale is also much longer than the typical radius of the electron cloud divided by the speed of light, and hence, the use of the electrostatic potential is also justified.

[6] The factor $|Z_{FI}|^2$ is missing in the cross section in [14–17].

JHEP03(2018)194

By using the dark matter velocity in the laboratory frame, $\mathbf{v}_{DM}^I$, the initial momentum in the center of the mass frame, $\mathbf{p}_I$, is given by

$$\mathbf{p}_{DM}^I = -\mathbf{p}_A^I = \mathbf{p}_I \simeq \mu_N \mathbf{v}_{DM}^I \,. \tag{3.36}$$

It should be noted that the scattering process is no longer elastic for $E_{ec}^F \neq E_{ec}^I$. Accordingly, the final state momentum in the center of the mass frame becomes smaller than $|\mathbf{p}_I|$;

$$|\mathbf{p}_F|^2 \simeq |\mathbf{p}_I|^2 - 2\mu_N (E_{ec}^F - E_{ec}^I) \,. \tag{3.37}$$

To satisfy $|\mathbf{p}_F| > 0$, there is a threshold velocity,

$$v_{DM}^{(th)} = \sqrt{\frac{2(E_{ec}^F - E_{ec}^I)}{\mu_N}} \,, \tag{3.38}$$

with which $|\mathbf{p}_F|$ is rewritten by

$$|\mathbf{p}_F| = \mu_N \sqrt{v_{DM}^2 - v_{DM}^{(th)\,2}} \,. \tag{3.39}$$

3.4 Atomic recoil spectrum

The atomic recoil spectrum in the laboratory frame is obtained as follows.[7] The atomic recoil energy E_R in the laboratory frame is given by

$$E_R = p_A^{F0} - m_A^F \simeq \frac{1}{2} \overline{m}_A v_F^2 \,. \tag{3.40}$$

As the momentum transfer is given by

$$\begin{aligned} q_A^2 &\simeq (|\mathbf{p}_F| - |\mathbf{p}_I|)^2 + 2|\mathbf{p}_I||\mathbf{p}_F|(1 - \cos\theta_{CM}) \,, & (3.41) \\ &\simeq -(E_{ec}^F - E_{ec}^I)^2 + 2 m_A E_R \simeq 2 m_A E_R \,, & (3.42) \end{aligned}$$

we obtain

$$E_R \simeq \frac{q_A^2}{2m_A} \simeq \frac{|\mathbf{p}_F|^2 + |\mathbf{p}_I|^2 - 2|\mathbf{p}_I||\mathbf{p}_F| \cos\theta_{CM}}{2m_A} \,. \tag{3.43}$$

Thus, the differential cross section with respect to the atomic recoil energy is given by

$$\begin{aligned} \frac{d\sigma}{dE_R} &\simeq \sum_{E_{ec}^F} \frac{1}{32\pi} \frac{m_A}{\mu_N^2 v_{DM}^2} \frac{|F_A(q_A^2)|^2 |\mathcal{M}(q_A)|^2}{(m_A + m_{DM})^2} |Z_{FI}(q_e)|^2 \,, & (3.44) \\ &\simeq \sum_{E_{ec}^F} \frac{1}{2} \frac{m_A}{\mu_N^2 v_{DM}^2} \tilde{\sigma}_N(q_A) |Z_{FI}(q_e)|^2 \,, & (3.45) \end{aligned}$$

where

$$q_e = m_e v_F \simeq \frac{m_e}{m_A} q_A \,. \tag{3.46}$$

[7] Similar kinematics has been discussed in the context of "inelastic excitation of nucleus" in [24, 25].

JHEP03(2018)194

Finally, the dark matter event rate for unit detector mass is given by

$$\frac{dR}{dE_R dv_{DM}} \simeq \frac{1}{m_A}\frac{\rho_{DM}}{m_{DM}}\frac{d\sigma}{dE_R} v_{DM}\tilde{f}_{DM}(v_{DM})\,, \tag{3.47}$$

$$\simeq \sum_{E_{ec}^F}\frac{1}{2}\frac{\rho_{DM}}{m_{DM}}\frac{1}{\mu_N^2}\tilde{\sigma}_N(q_A)\times|Z_{FI}(q_e)|^2\times\frac{\tilde{f}(v_{DM})}{v_{DM}}\,. \tag{3.48}$$

Here, ρ_{DM} denotes the local dark matter density[8] and $\tilde{f}(v_{DM})$ is the dark matter velocity distribution integrated over the directional component normalized by[9]

$$\int \tilde{f}_{DM}(v_{DM})\,dv_{DM} = 1\,. \tag{3.49}$$

4 Migdal effect in single electron approximation

4.1 Single electron wave function

In our numerical calculation, we use the electron wave function, $\Phi_{E_{ec}}$, obtained by the Dirac-Hartree-Fock method, where the relativistic effects on the electron cloud are taken into account (see e.g. [28] for review).

In the Dirac-Hartree-Fock approximation, an electron state is given by a Slater determinant made up of one orbital per each electron in an averaged central potential around a nucleus. In this approximation, the energy eigenstates in eq. (2.21) are approximated by

$$\Psi_{E_A}(\mathbf{x}_N,\{\mathbf{x}\}) \simeq e^{i\mathbf{p}_N\cdot\mathbf{x}_N}\sum_{\sigma\in S_{N_e}}\frac{\mathrm{sgn}(\sigma)}{\sqrt{N_e!}}e^{i\mathbf{q}_e\cdot\mathbf{x}_1}\phi^{\alpha_1}_{o_{\sigma(1)}}(\mathbf{x}_1-\mathbf{x}_N)e^{i\mathbf{q}_e\cdot\mathbf{x}_2}\phi^{\alpha_2}_{o_{\sigma(2)}}(\mathbf{x}_2-\mathbf{x}_N)$$
$$\times\cdots e^{i\mathbf{q}_e\cdot\mathbf{x}_{N_e}}\phi^{\alpha_{N_e}}_{o_{\sigma(N_e)}}(\mathbf{x}_{N_e}-\mathbf{x}_N)\,, \tag{4.1}$$

where S_{N_e} denotes the permutation group of degree N_e. Here we explicitly show the indices of the Dirac spinor by $\alpha_i = 1\cdots 4$, which are encapsulated in $\{\mathbf{x}\}$ on the left-hand side.

The electron cloud consists of the N_e orbitals,[10]

$$ec = \{o_1, o_2, \cdots o_{N_e}\}\,, \tag{4.2}$$

where each orbital is specified by energy E, relativistic angular momentum κ, and magnetic quantum number m,[11]

$$o_i = (E_i, \kappa_i, m_i)\,. \tag{4.3}$$

For a bounded electron, i.e. $E_i < 0$, the state is classified by the principle quantum number, n_i, while the spectrum is continuous for an unbounded electron, i.e. for $E_i > 0$.

[8] For the Burkert profile [7], for example, it is estimated to be $\rho_{DM} \simeq 0.487^{+0.075}_{-0.088}\,\mathrm{GeV/cm^3}$.

[9] For astrophysical uncertainties of the direct detection experiments (see e.g. [26, 27]).

[10] The Slater determinant in eq. (4.1) is reducible in terms of the total angular momentum of the atom.

[11] The value κ determines both the total angular momentum j and the orbital angular momentum ℓ via $\kappa = \mp(j+1/2)$ for $j = \ell \pm 1/2$.

JHEP03(2018)194

The one electron Dirac orbital $\phi_o^\alpha(\mathbf{x}_i)$ is given by using the two-component spherical spinors $\Omega_{\kappa m}$;

$$\phi_o(\mathbf{x}) = \frac{1}{r}\begin{pmatrix} P_E(r)\Omega_{\kappa m}(\theta,\varphi) \\ iQ_E(r)\Omega_{-\kappa m}(\theta,\varphi)\end{pmatrix}. \tag{4.4}$$

See e.g. [28] for the details of the spherical spinors and the radial wave functions, $P_E(r)$ and $Q_E(r)$. Here, an atom is at rest and r denotes the distance between the electron and the center of the potential. The one-electron states are normalized such that

$$\sum_{\alpha=1}^{4}\int d^3\mathbf{x}\,\phi_o(\mathbf{x})^{\alpha *}\phi_{o'}^{\alpha}(\mathbf{x}) = \begin{cases}\delta_{nn'}\delta_{\kappa\kappa'}\delta_{mm'} & \text{(bounded)} \\ (2\pi)\delta(E-E')\delta_{\kappa\kappa'}\delta_{mm'} & \text{(unbounded)}\end{cases}. \tag{4.5}$$

In the Dirac-Hartree-Fock approximation, the electron cloud transition factor in eq. (3.30) is rewritten by

$$Z_{FI}(\mathbf{q}_e) = \sum_{\sigma\in S_{N_e}}\mathrm{sgn}(\sigma)\prod_{i=1}^{N_e}\sum_{\alpha_i=1}^{4}\int d^3\mathbf{x}_i\,\phi_{o^F_{\sigma(i)}}^{\alpha_i *}(\mathbf{x}_i)e^{-i\mathbf{q}_e\cdot\mathbf{x}_i}\phi_{o_i^I}^{\alpha_i}(\mathbf{x}_i)\,. \tag{4.6}$$

In this approximation, the transition amplitude is given by the product of the transition amplitudes between the electron orbitals.

4.2 Single electron excitation/ionization

For an atomic recoil with a momentum transfer smaller than the hundreds MeV range, the factor $|\mathbf{q}_e\cdot\mathbf{x}_i|$ is expected to be small than $\mathcal{O}(1)$ on the atomic scale.[12] Thus, we consider the Migdal effect at the leading order of q_e. At the leading order of q_e, only one electron can be excited/ionized, and hence, the initial and the final state configurations are

$$ce_I = \{o_1,\cdots,o_k,\cdots o_{N_e}\}\,, \tag{4.7}$$

$$ce_F = \{o_1,\cdots,o'_k,\cdots o_{N_e}\}\,, \tag{4.8}$$

where

$$E^F_{ec} - E^I_{ec} \simeq E'_k - E_k\,. \tag{4.9}$$

Hereafter, we assume that the initial electron cloud stays in the ground state, where all the electrons are bounded by the Coulomb potential of the nucleus. In the final electron state, o'_k can be either a bounded or an unbounded orbital.

At the leading order of q_e, the electron cloud transition amplitude is reduced to

$$Z_{FI}(\mathbf{q}_e) = z_{\mathbf{q}_e}(E'_k,\kappa'_k,m'_k|E_k,\kappa_k,m_k) = -i\sum_{\alpha_k=1}^{4}\int d^3\mathbf{x}_k\,\phi_{o'_k}^{\alpha_k *}(\mathbf{x}_k)(\mathbf{q}_e\cdot\mathbf{x}_k)\phi_{o_k}^{\alpha_k}(\mathbf{x}_k)\,. \tag{4.10}$$

[12] For $v_F \simeq 10^{-3}$, for example, $q_e \simeq 0.5\,\mathrm{keV}$ and hence $|\mathbf{q}_e\cdot\mathbf{x}_i| \ll 1$ even for a Bohr radius.

JHEP03(2018)194

	$1s$	$2s$	$2p$	$3s$	$3p$	$3d$	$4s$	$4p$	$4d$	$4f$	$5s$	$5p$
Na	2	2	6	1	0	0	0	0	0	0	0	0
Ar	2	2	6	2	6	0	0	0	0	0	0	0
Ge	2	2	6	2	6	10	2	2	0	0	0	0
I	2	2	6	2	6	10	2	6	10	0	2	5
Xe	2	2	6	2	6	10	2	6	10	0	2	6

Table 1. The number of electrons in a shell for the ground state configurations.

At this order, electron transitions are allowed only when the orbital angular momenta of o'_k and o_k differ by one, i.e. $|\ell'_k - \ell_k| = 1$. Thus, the transition amplitude is reduced to

$$z_{\mathbf{q}_e}(E'_k, \kappa'_k, m'_k | E_k, \kappa_k, m_k) = -iq_e \int dr\, r \times \left[P_{E'_k}(r) P_{E_k}(r) + Q_{E'_k}(r) Q_{E_k}(r) \right] \times \int d\Omega\, \Omega^\dagger_{\kappa',m'}(\theta,\varphi) \cos\theta\, \Omega^\dagger_{\kappa,m}(\theta,\varphi) \ . \tag{4.11}$$

Here, we take the quantization axis of the angular momentum corresponds to $\mathbf{q}_e$. The angle, θ, is the one between $\mathbf{q}_e$ and $\mathbf{x}_e$. The choice of the quantization is irrelevant for the final results as we take an average/sum the magnetic quantum numbers of the electrons in the initial/final states.

In the following discussion, we only require an accuracy of $\mathcal{O}(10)\%$ for the electron binding energies. For this accuracy, the bound state energies for given principal number and the orbital angular momentum are not distinguishable, and hence, it is useful to label the bound states by (n, ℓ). Accordingly, the transition rates are also labeled by (n, ℓ),

$$\sum_F |Z_{FI}|^2 = |Z_{II}|^2 + \sum_{n,\ell,n',\ell'} p^d_{q_e}(n\ell \to n'\ell') + \sum_{n,\ell} \int \frac{dE_e}{2\pi} \frac{d}{dE_e} p^c_{q_e}(n\ell \to E_e) \, . \tag{4.12}$$

Here, $|Z_{II}|^2 \simeq 1 + \mathcal{O}(q_e^2 \langle r \rangle^2)$ is the probability for the electrons unaffected by the nuclear recoil (see also appendix B for discussion of the probability conservation). The excitation and the ionization probabilities, $p^d_{q_e}$ and $p^c_{q_e}$, are defined by

$$p^d_{q_e}(n\ell \to n'\ell') = \frac{\omega^{\max}_{\ell'} - \omega_{n',\ell'}}{\omega^{\max}_{\ell'}} \frac{\omega_{n,\ell}}{\omega^{\max}_{\ell}} \sum_{\kappa,\kappa',m,m'} \delta_{\ell,|\kappa+1/2|-1/2} \delta_{\ell',|\kappa'+1/2|-1/2} \times \left| z_{\mathbf{q}_e}(E_{n'\kappa'}, \kappa', m' | E_{n\kappa}, \kappa, m) \right|^2 \ , \tag{4.13}$$

$$\frac{d}{dE_e} p^c_{q_e}(n\ell \to E_e) = \frac{\omega_{n,\ell}}{\omega^{\max}_{\ell}} \sum_{\kappa,\kappa',m,m'} \delta_{\ell,|\kappa+1/2|-1/2} \left| z_{\mathbf{q}_e}(E_e, \kappa', m' | E_{n\kappa}, \kappa, m) \right|^2 \ . \tag{4.14}$$

Here, $E_{n\kappa}$ is the size of the binding energy for the bounded electron labeled by (n, κ), E_e the energy of the unbounded electron, $\omega_{n\ell}$ the occupation number of the subshell (see table 1), and $\omega^{\max}_\ell = 2(2\ell + 1)$. The final state orbital angular momentum, i.e. $\ell' = \ell \pm 1$, is summed implicitly in eq. (4.14).

JHEP03(2018)194

4.3 Ionization spectrum at the leading order

By combining eqs. (3.48) and (4.12), we find that the ionized electron spectrum from an initial orbital o_k is given by

$$\frac{dR}{dE_R\, dE_e\, dv_{DM}} \simeq \frac{dR_0}{dE_R\, dv_{DM}} \times \frac{1}{2\pi} \sum_{n,\ell} \frac{d}{dE_e} p^c_{q_e}(n\ell \to E_e)\,, \tag{4.15}$$

$$\frac{dR_0}{dE_R\, dv_{DM}} \simeq \frac{1}{2} \frac{\rho_{DM}}{m_{DM}} \frac{1}{\mu_N^2} \tilde{\sigma}_N(q_A) \times \frac{\tilde{f}(v_{DM})}{v_{DM}}\,. \tag{4.16}$$

Here,

$$E_R \simeq \frac{q_A^2}{2m_A}\,, \quad q_e \simeq \frac{m_e}{m_A} q_A\,. \tag{4.17}$$

It should be noted that the atomic recoil energy, E_R, and the electron transition energy, ΔE, are correlated through the energy-momentum conservation;

$$E_R = \frac{\mu_N^2}{2m_N} v_{DM}^2 \left(\left(1 - \sqrt{1 - \frac{2\Delta E}{\mu_N v_{DM}^2}} \right)^2 + 2(1 - \cos\theta_{CM}) \sqrt{1 - \frac{2\Delta E}{\mu_N v_{DM}^2}} \right), \tag{4.18}$$

where

$$\Delta E = E_e + E_{n\ell}\,, \tag{4.19}$$

$$E_{n\ell} = \frac{1}{2} \sum_{\kappa} \delta_{\ell,|\kappa+1/2|-1/2} E_{n\kappa}\,. \tag{4.20}$$

From this expression, we find the minimum dark matter velocity for given E_R and ΔE,

$$v_{DM,\mathrm{min}} \simeq \frac{m_N E_R + \mu_N \Delta E}{\mu_N \sqrt{2\, m_N E_R}}\,. \tag{4.21}$$

In figure 1, we show the minimum velocity as a function of E_R for isolated Ar and Xe atoms. We also show the kinematically allowed region of E_R and ΔE for Ar and Xe atoms for $v_{DM} = 10^{-3}$ in figure 2.

It should be also noted that there is a kinematical upper limit on the electron transition energy, ΔE, for a given speed of dark matter, which is set by eq. (3.38),

$$\Delta E_{\mathrm{MAX}} = \frac{1}{2} \mu_N v_{DM}^2\,. \tag{4.22}$$

In figure 3, we show ΔE_{MAX} as a function of v_{DM}. The figure shows that ΔE in the keV range is kinematically allowed for $v_{DM} \gtrsim 10^{-3}$. It is also notable that, for $\Delta E = \Delta E_{\mathrm{MAX}}$, the atomic recoil energy is given by

$$E_R = \frac{\mu_N^2}{2m_N} v_{DM}^2 = \frac{\mu_N}{m_N} \times \Delta E_{\mathrm{MAX}}\,. \tag{4.23}$$

Thus the corresponding atomic recoil energy is smaller than ΔE_{MAX}, which plays an important role on the dark matter detections as discussed in the later section.

JHEP03(2018)194

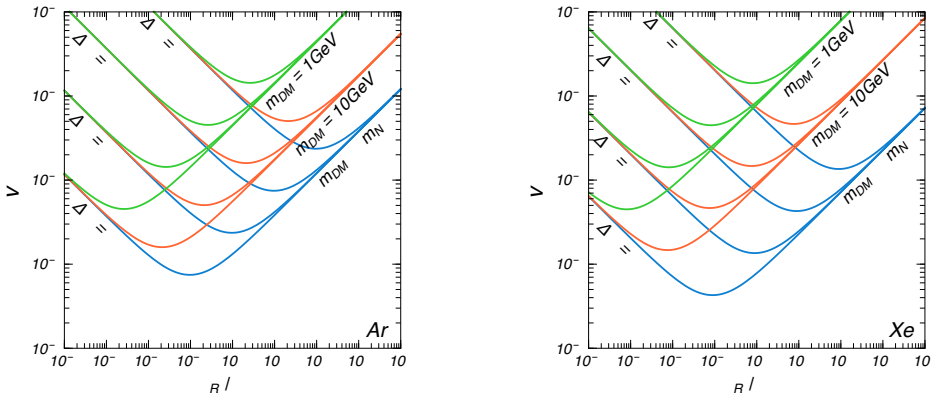

Figure 1. The minimum dark matter velocity as a function of the atomic recoil energy E_R for given ΔE and m_{DM} for Ar and Xe.

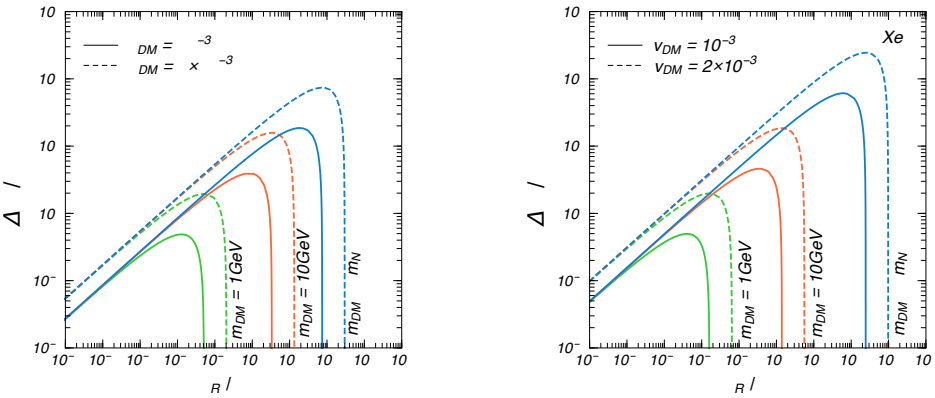

Figure 2. Kinematical constraints on the plane of $(E_R, \Delta E)$ for given m_{DM} and v_{DM} for Ar and Xe atoms. The regions below the lines are kinematically allowed.

When electrons are emitted from inner orbitals, the created core-holes are de-excited subsequently.[13] The typical timescales of the de-excitation processes are of $\mathcal{O}(10)$ fs. Thus, the energies of the electron emission and the de-excitation are measured simultaneously, and hence, the total electronic energy released at the ionization is given by

$$E_{EM} = E_e + E_{\rm dex}\,, \tag{4.24}$$

where $E_{\rm dex}$ is the energy released at the de-excitation.

Accordingly, the electromagnetic energy spectrum is given by

$$\frac{dR}{dE_R\, dE_{EM}\, dv_{DM}} \simeq \frac{dR_0}{dE_R\, dv_{DM}} \times \frac{1}{2\pi} \sum_{n,\ell} \frac{d}{dE_e} p^c_{q_e}(n\ell \to (E_{EM} - E_{n\ell}))\,. \tag{4.25}$$

[13]The de-excitation proceeds through the X-ray transition, the Auger transition, or the Coster-Kronig transition (see [29, 30] for review, see also [31]). For a core-hole in $n > 1$ states the Coster-Kroning transition dominates the de-excitation process.

JHEP03(2018)194

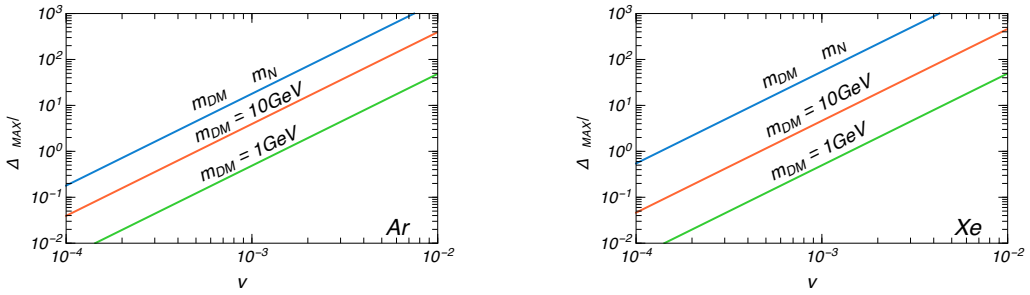

Figure 3. The kinematical upper limits on the electron transition energy, ΔE, as a function of the speed of dark matter for a given m_{DM}. In the solar rest frame, typical dark matter velocities are of 500 km/s with an upper limit of around 700 km/s.

Hereafter, we simply assume that the ionization energy is released completely, that is $E_{EM} = \Delta E$.[14] One caveat here is that E_{EM} is not the energy of a single electron/photon but the collection of the energies of the electrons and photons emitted at the de-excitation and the ionization. Thus, the detector responses to E_{EM} might be different from those to a single electron/photon with the same energy, although we do not take such effects into account in the following discussion.

Similarly, the excited atoms also lead to electronic energy release by de-excitation. Assuming the complete de-excitation again, we obtain the electromagnetic energy spectrum;

$$\frac{dR}{dE_R\, dE_{EM}\, dv_{DM}} \simeq \frac{dR_0}{dE_R\, dv_{DM}} \times \sum_{n,n',\ell,\ell'} p^d_{q_e}(n\ell \to n'\ell') \times \delta(E_{EM} - \Delta E_{n\ell\to n'\ell'})\,. \quad (4.26)$$

Here $\Delta E_{n\ell\to n'\ell'}$ is given by

$$\Delta E_{n\ell\to n'\ell'} = \frac{1}{2}\sum_{\kappa} \delta_{\ell,|\kappa+1/2|-1/2} E_{n\kappa} - \frac{1}{2}\sum_{\kappa'} \delta_{\ell',|\kappa'+1/2|-1/2} E_{n'\kappa'}\,. \quad (4.27)$$

5 Numerical analysis

In this section, we provide numerical estimates of the electron transition probabilities, p^d_q and p^c_q, for isolated Ar, Ge, Xe, Na, and I atoms. To calculate the electron wave functions, we use the `Flexible Atomic Code (FAC, cFAC)` [32]. It is a multi-configuration Dirac-Fock (MCDF) program to calculate various atomic radiative and collisional processes. We give a brief review of the Dirac-Hartree-Fock method in appendix C. In `FAC`, all of the single electron wave functions, including those of excited and unboudend electrons, are calculated from a universal central potential,

$$V(\mathbf{x} - \mathbf{x}_N) \simeq V_N(r) + V_{ee}(r)\,, \quad (5.1)$$

$$V_{ee}(r) = \frac{\alpha \sum_{n,\kappa} \omega_{n\kappa}\rho_{n\kappa}(r)\mathcal{Q}^{\rm eff}_{n\kappa}(r)}{r\sum_{n,\kappa}\omega_{n\kappa}\rho_{n\kappa}(r)}\,, \quad (5.2)$$

[14] If the atom is completely isolated, the ionization and the subsequent Auger and Coster-Kronig transitions leave ionized atoms. In the medium, on the contrary, ionized atoms are also de-excited eventually.

JHEP03(2018)194

which is optimized for the (possible) ground state configurations. Here, $V_N(r)$ denotes the Coulomb potential from the nucleus, and α the fine-structure constant. The factor $\mathcal{Q}^{\rm eff}_{n\kappa}$ provides the effective charge of the central potential for the electrons in the $n\kappa$-orbital;

$$\begin{aligned}\mathcal{Q}^{\rm eff}_{n\kappa}(r) = &\sum_{n',\kappa'} \omega_{n'\kappa'} Y^0_{n'\kappa'}(r) - Y^0_{n\kappa}(r) \\ &- (\omega_{n\kappa} - 1) \sum_{k>0} f_k(\kappa) Y^k_{n\kappa}(r) \\ &- \sum_{n'\kappa' \neq n\kappa} \frac{\rho_{n\kappa,n'\kappa'}\omega_{n\kappa}\omega_{n'\kappa'}}{\rho_{n\kappa}\omega_{n\kappa}} \sum_k g_k(\kappa,\kappa') Y^k_{n\kappa,n'\kappa'}(r)\,. \end{aligned} \tag{5.3}$$

Here, $\omega_{n\kappa}$ is the occupation number of the subshell, $\rho_{n\kappa} = \rho_{n\kappa,n\kappa}$, $Y^k_{n\kappa} = Y^k_{n\kappa,n\kappa}$, and

$$\rho_{n\kappa,n'\kappa'}(r) = P_{n\kappa}(r)P_{n'\kappa'}(r) + Q_{n\kappa}(r)Q_{n'\kappa'}(r)\,, \tag{5.4}$$

$$Y^k_{n\kappa,n'\kappa'}(r) = r\int \frac{r^k_<}{r^{k+1}_>}\rho_{n\kappa,n'\kappa'}(r')dr'\,, \tag{5.5}$$

$$f_k(\kappa) = \left(1 + \frac{1}{2j_\kappa}\right)\begin{pmatrix} j_\kappa & k & j_\kappa \\ -1/2 & 0 & 1/2\end{pmatrix}^2, \tag{5.6}$$

$$g_k(\kappa,\kappa') = \begin{pmatrix} j_\kappa & k & j_{\kappa'} \\ -1/2 & 0 & 1/2\end{pmatrix}^2, \tag{5.7}$$

where j_κ is the value of j corresponding to κ, $r_> = \max(r,r')$, $r_< = \min(r,r')$, and $\begin{pmatrix} j_1 & j_2 & j_3 \\ m_1 & m_2 & m_3\end{pmatrix}$ is the Wigner $3j$ symbol.

Due to the universal central potential, the wave functions of orbitals obtained by `FAC` are orthogonal to each other, and hence, they can be used to calculate the transition rates in the previous sections. In our analysis, we further approximate the atomic state by a single Slater determinant of the wave functions labeled by a set of $\{n,\kappa,m\}$. The energy eigenvalues obtained with this approximation reproduce the measured values in ref. [33] at the accuracy better than 20%, which is good enough for later discussion (see the energy levels in table 2).

5.1 Transition probabilities

We show the numerical results of the transition probabilities to the order of $O(q_e^2)$. The ground state of the atom consists of a complex of the orbitals given in table 1. If there are more than one energy eigenstate configurations for a given complex, we take an average of the transition probabilities for those energy eigenstate configurations. As discussed in section 4.2, we consider the final states in which only one of o_k's in the initial state is replaced by an excited or an unbouded electron state.

In figure 4, we show the differential ionization probabilities, $dp^c_{q_e}/dE_e$, for $q_e = m_e v_F$ with $v_F = 10^{-3}$. In the figure, we sum all the contributions from different orbital angular momenta in the initial state, ℓ, for a given principal quantum number, n. We also sum all the possible final states for a given n. It should be noted that the spectrum shape of $dp^c_{q_e}/dE_e$ does not depend on v_F, and hence, the probabilities for a different q_e is obtained

JHEP03(2018)194

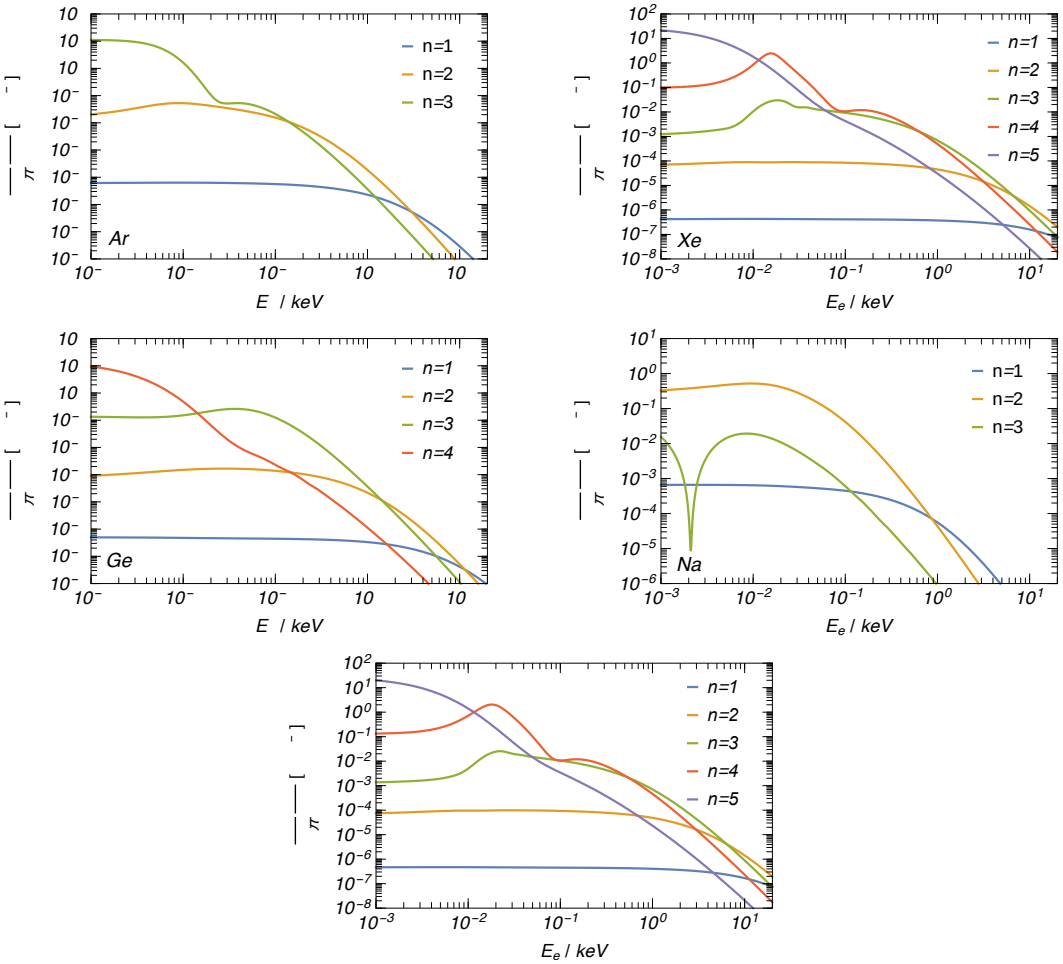

Figure 4. The differential ionization probabilities as a function of the emitted electron energy, E_e, for isolated Ar, Xe, Ge, Na, and I. The contributions from different ℓ's are summed. We also summed all the possible final states for a given n. The integrated probabilities are given in table 2.

by multiplying $q_e^2/(m_e \times 10^{-3})^2$. The integrated probabilities are also given in table 2 for a given initial (n, ℓ). The results show that the ionization probabilities from the inner shells can be of $\mathcal{O}(10^{-2})$ for $v_F = 10^{-3}$. The ionization probabilities from the valence electrons can be even of $\mathcal{O}(10^{-1})$.

As we have seen in figure 2, the recoil energy E_R and the electron excitation energy ΔE (and hence E_e) are kinematically constrained for given m_{DM} and v_{DM}. Cross correlations of the ionization probabilities between E_R and E_e are obtained by rescaling the results in figure 4 by $q_e^2 = 2m_e^2 E_R/m_A$ within the kinematically allowed region in figure 2.

In table 2, we also show the excitation probabilities, $p^d_{q_e}(n\ell \to n'\ell')$. As the table shows, the excitation probabilities are much smaller than the ionization probabilities for a given initial n.

Before closing this section, let us comment on the probability conservation in the single electron transition. As discussed in the appendix B, the single electron transition

JHEP03(2018)194

probability satisfies,

$$\frac{1}{\omega_{n,\ell}}\left(\sum_{n',\ell'} p^{d}_{q_e}(n\ell \to n'\ell') + \int \frac{dE_e}{2\pi}\frac{d}{dE_e} p^{c}_{q_e}(n\ell \to E_e)\right) = 1 - p_{\rm unchanged}(n\ell) - p_{\rm occupied}(n\ell)\,. \tag{5.8}$$

Here, $p_{\rm unchanged}$ and $p_{\rm occupied}$ are given in eqs. (B.6) and (B.8), while the lefthand side corresponds to $p_{\rm ex}(n\ell)$ in eq. (B.7) (see also eqs. (4.13) and (4.14)). In our analysis, we numerically checked that $p_{\rm unchanged}$, $p_{\rm occupied}$, and $p_{\rm ex}$ satisfy the probability conservation in eq. (5.8).[15]

In ref. [18], the probability $p_{\rm occupied}$ ($P^1_{exc,i}$ in ref. [18]) is incorrectly defined, which is related to $p_{\rm occupied}$ in this paper by

$$p_{\rm occupied}\big|_{[15]} = p_{\rm occupied} \times (1 - p_{\rm unchanged})\,. \tag{5.9}$$

Since $p_{\rm unchanged} \simeq 1$, $p_{\rm occupied}\big|_{[15]}$ is much smaller than $p_{\rm occupied}$. The ionization probability in ref. [18] is, on the other hand, estimated by using the (incorrect) probability conservation,[16]

$$p_{\rm ionization}\big|_{[15]} = 1 - p_{\rm unchanged} - p_{\rm occupied}\big|_{[15]} - \frac{1}{\omega_{n,\ell}}\sum_{n',\ell'} p^{d}_{q_e}(n\ell \to n'\ell')\,. \tag{5.10}$$

Since we find $p_{\rm occupied} \gtrsim p_{\rm ex}$ numerically, it shows that the ionization rates in ref. [18] are overestimated.

Ar ($q_e = m_e \times 10^{-3}$)

(n,ℓ)	$\mathcal{P}_{\to 3d}$	$\mathcal{P}_{\to 4s}$	$\mathcal{P}_{\to 4p}$	$\mathcal{P}_{\to 4d}$	$\mathcal{P}_{\to 5s}$	$\mathcal{P}_{\to 5p}$	$E_{n\ell}$ [eV]	$\frac{1}{2\pi}\int dE_e \frac{dp^c}{dE_e}$
$1s$	–	–	1.3×10^{-7}	–	–	4.3×10^{-8}	3.2×10^{3}	7.2×10^{-5}
$2s$	–	–	5.3×10^{-6}	–	–	1.8×10^{-6}	3.0×10^{2}	4.1×10^{-4}
$2p$	4.3×10^{-6}	5.0×10^{-6}	–	3.0×10^{-6}	1.3×10^{-6}	–	2.4×10^{2}	4.2×10^{-3}
$3s$	–	–	5.3×10^{-7}	–	–	1.1×10^{-6}	2.7×10	1.2×10^{-3}
$3p$	7.9×10^{-3}	8.5×10^{-3}	–	4.0×10^{-3}	1.2×10^{-3}	–	1.3×10	7.4×10^{-2}

(n,ℓ)	$3d$	$4s$	$4p$	$4d$	$5s$	$5p$
$E_{n\ell}$[eV]	1.6	3.7	2.5	0.88	1.6	1.2

(Table 2. Cont.)

[15] Numerically, $p_{\rm occupied}$ is at the same order or even an order of magnitude larger than $p_{\rm ex}$.

[16] The one electron transition probabilities in this paper correspond to $p_{\rm unchanged} = P^1_{ii}$, $p_{\rm occupied} = P^1_{exc,i}$, and $P^1_{bound,i} = \sum_{n',\ell'} p^{d}_{q_e}(n\ell \to n'\ell')/\omega_{n,\ell}$.

JHEP03(2018)194

Xe ($q_e = m_e \times 10^{-3}$)

(n,ℓ)	$\mathcal{P}_{\to 4f}$	$\mathcal{P}_{\to 5d}$	$\mathcal{P}_{\to 6s}$	$\mathcal{P}_{\to 6p}$	$E_{n\ell}$ [eV]	$\frac{1}{2\pi}\int dE_e \frac{dp^c}{dE_e}$
1s	–	–	–	7.3×10^{-10}	3.5×10^{4}	4.6×10^{-6}
2s	–	–	–	1.8×10^{-8}	5.4×10^{3}	2.9×10^{-5}
2p	–	3.0×10^{-8}	6.5×10^{-9}	–	4.9×10^{3}	1.3×10^{-4}
3s	–	–	–	2.7×10^{-7}	1.1×10^{3}	8.7×10^{-5}
3p	–	3.4×10^{-7}	4.0×10^{-7}	–	9.3×10^{2}	5.2×10^{-4}
3d	2.3×10^{-9}	–	–	4.3×10^{-7}	6.6×10^{2}	3.5×10^{-3}
4s	–	–	–	3.1×10^{-6}	2.0×10^{2}	3.4×10^{-4}
4p	–	4.1×10^{-8}	3.0×10^{-5}	–	1.4×10^{2}	1.4×10^{-3}
4d	7.0×10^{-7}	–	–	1.5×10^{-4}	6.1×10	3.4×10^{-2}
5s	–	–	–	1.2×10^{-4}	2.1×10	4.1×10^{-4}
5p	–	3.6×10^{-2}	2.1×10^{-2}	–	9.8	1.0×10^{-1}

(n,ℓ)	$4f$	$5d$	$6s$	$6p$
$E_{n\ell}$[eV]	0.85	1.6	3.3	2.2

Ge ($q_e = m_e \times 10^{-3}$)

(n,ℓ)	$\mathcal{P}_{\to 4p}$	$\mathcal{P}_{\to 4d}$	$\mathcal{P}_{\to 5s}$	$\mathcal{P}_{\to 5p}$	$\mathcal{P}_{\to 6s}$	$E_{n\ell}$ [eV]	$\frac{1}{2\pi}\int dE_e \frac{dp^c}{dE_e}$
1s	5.0×10^{-8}	–	–	7.9×10^{-9}	–	1.1×10^{4}	1.8×10^{-5}
2s	1.8×10^{-6}	–	–	2.8×10^{-7}	–	1.4×10^{3}	1.2×10^{-4}
2p	–	3.3×10^{-7}	1.1×10^{-7}	–	3.4×10^{-8}	1.2×10^{3}	6.9×10^{-4}
3s	3.7×10^{-5}	–	–	5.6×10^{-6}	–	1.7×10^{2}	5.4×10^{-4}
3p	–	6.0×10^{-9}	2.8×10^{-5}	–	8.3×10^{-6}	1.2×10^{2}	2.4×10^{-3}
3d	2.3×10^{-3}	–	–	2.3×10^{-4}	–	3.5×10	2.8×10^{-2}
4s	4.0×10^{-2}	–	–	3.9×10^{-4}	–	1.5×10	5.3×10^{-4}
4p	-	2.7×10^{-2}	1.6×10^{-2}	–	1.5×10^{-3}	6.5	3.7×10^{-2}

(n,ℓ)	$4d$	$5s$	$5p$	$6s$
$E_{n\ell}$[eV]	1.6	3.0	2.0	1.4

(Table 2. Cont.)

JHEP03(2018)194

Na ($q_e = m_e \times 10^{-3}$)

(n,ℓ)	$\mathcal{P}_{\to 3s}$	$\mathcal{P}_{\to 3p}$	$\mathcal{P}_{\to 3d}$	$\mathcal{P}_{\to 4s}$	$\mathcal{P}_{\to 4p}$	$\mathcal{P}_{\to 4d}$	$E_{n\ell}$ [eV]	$\frac{1}{2\pi}\int dE'_k \frac{dp^c}{dE'_k}$
1s	–	2.1×10^{-6}	–	–	6.4×10^{-7}	–	1.1×10^{3}	2.5×10^{-4}
2s	–	6.8×10^{-5}	–	–	2.0×10^{-5}	–	6.5×10	1.7×10^{-3}
2p	5.9×10^{-5}	–	1.1×10^{-4}	1.5×10^{-4}	–	6.2×10^{-5}	3.8×10	2.2×10^{-2}
3s	-	8.8×10^{-2}	–	–	1.1×10^{-3}	–	6.1	5.7×10^{-4}

(n,ℓ)	$3p$	$3d$	$4s$	$4p$	$4d$
$E_{n\ell}$[eV]	3.3	1.5	2.1	1.5	0.86

I ($q_e = m_e \times 10^{-3}$)

(n,ℓ)	$\mathcal{P}_{\to 4f}$	$\mathcal{P}_{\to 5p}$	$\mathcal{P}_{\to 5d}$	$\mathcal{P}_{\to 6s}$	$\mathcal{P}_{\to 6p}$	$E_{n\ell}$ [eV]	$\frac{1}{2\pi}\int dE_e \frac{dp^c}{dE_e}$
1s	–	2.0×10^{-9}	–	–	7.8×10^{-10}	3.3×10^{4}	5.1×10^{-6}
2s	–	5.0×10^{-8}	–	–	2.0×10^{-8}	5.1×10^{3}	3.1×10^{-5}
2p	–	–	3.3×10^{-8}	6.9×10^{-9}	–	4.6×10^{3}	1.4×10^{-4}
3s	–	7.7×10^{-7}	–	–	3.0×10^{-7}	1.0×10^{3}	1.2×10^{-4}
3p	–	–	3.8×10^{-7}	4.4×10^{-7}	–	8.7×10^{2}	6.4×10^{-4}
3d	1.7×10^{-9}	1.3×10^{-6}	–	–	5.0×10^{-7}	6.1×10^{2}	3.5×10^{-3}
4s	–	9.2×10^{-6}	–	–	3.4×10^{-6}	1.8×10^{2}	3.8×10^{-4}
4p	–	–	1.6×10^{-7}	3.6×10^{-5}	–	1.3×10^{2}	1.5×10^{-3}
4d	9.8×10^{-7}	7.7×10^{-4}	–	–	2.0×10^{-4}	5.1×10	5.2×10^{-2}
5s	–	8.9×10^{-3}	–	–	1.8×10^{-4}	1.9×10	4.3×10^{-4}
5p	–	-	4.0×10^{-2}	2.2×10^{-2}	–	8.8	8.8×10^{-2}

(n,ℓ)	$4f$	$5d$	$6s$	$6p$
$E_{n\ell}$[eV]	0.85	1.6	3.2	2.1

Table 2. The excitation probabilities for a given initial state (n, ℓ). $\mathcal{P}_{\to n'\ell'}$ is defined by $\mathcal{P}_{\to n'\ell'} \equiv p^d_{q_e}(n\ell \to n'\ell')$. The probabilities not shown in this table are forbidden or negligibly small. The integrated ionization probabilities are also shown in the rightmost column. The averaged binding energies of the initial and the final orbitals are also shown which are obtained by `FAC`.

JHEP03(2018)194

6 Effects on dark matter direct detection

As we have shown in the previous sections, a nuclear recoil is accompanied by the ionization and the excitation of the atom through the Migdal effect. The electric energy released by the ionization and the de-excitation can be in the keV range when the incident dark matter velocity exceeds the threshold in eq. (3.38).

In this section, we discuss how those electronic energy injections affect the dark matter signals at direct detection experiments. In our analysis, we have assumed isolated atoms. Thus, the results in the previous section are not directly applicable to the non-isolated atoms in liquid or crystals. For example, the energy levels of the valence electrons are affected by the ambient atoms by $\mathcal{O}(0.1)\,\mathrm{eV}$.[17] Furthermore, when the electronic band structure is formed in the medium, the excitations into the unoccupied state should be reinterpreted as transitions into the conducting band.

The ionization rates from the inner orbitals are, on the other hand, expected to be less affected by the ambient atoms. In fact, the binding energies of the inner orbital are much larger than eV, and hence, the relevant length scales for the transition factors, z_e, are much smaller than the typical distance between atoms. Thus, the ionization spectrum in eq. (4.15) can be applied rather reliably for the ones from the inner orbitals.[18] In the following, we confine our arguments to liquid Xe detectors.

6.1 Migdal effects on the recoil spectrum

In the absence of the Migdal effect, the liquid Xe detectors respond to the nuclear recoil roughly through the following steps [35–37]. After the nuclear recoil, the electron clouds are assumed to catch up with the nucleus immediately, so that the atom remains neutral. The recoil "atom" loses its energy through scattering with adjacent atoms in the medium where the inelastic scatterings involve the ionization and excitation of the atoms. These processes continue until the scattered atoms are thermalized. Eventually, a fraction of the initial recoil energy E_R is converted to the measurable electronic excitation while the rest is lost into the heat of the medium [38–41].

This should be contrasted with the electron recoils caused by incident gamma or beta rays, where the entire recoil energy is transferred to the measurable electronic excitation. Conventionally, the calibrated nuclear recoil energy, E_{nr}, and the electron equivalent energy, E_{ee}, measured by the scintillation photons are related by[19]

$$E_{nr} = \frac{E_{ee}}{\mathcal{L}_{\mathrm{eff}}} \cdot \frac{S_e}{S_n} \,. \tag{6.1}$$

Here, $\mathcal{L}_{\mathrm{eff}}$ is defined as the ratio between E_{ee} and E_{nr} at zero drift field relative to 122 keV gamma rays, which is $\mathcal{L}_{\mathrm{eff}} \simeq 0.1$–$0.2$ for $E_{nr} \lesssim 100\,\mathrm{keV}$ [42–45]. The quantities, S_e and S_n, are the scintillation quenching factors of electron and nuclear recoils due to the drift electric field, E_d, which are $S_e \simeq 0.4$–1 [46] and $S_n \simeq 1$ [47] for $E_d \leq 4\,\mathrm{kV/cm}$, respectively.[20]

[17] For the energy levels of the valence electrons of the liquid Xe, see e.g. ref. [34].

[18] As it is highly difficult to quantify the uncertainties from the effects of the ambient atoms, it is desirable to test the Migdal effect experimentally via the low energy nuclear recoils with $E_R \ll \mathcal{O}(1)\,\mathrm{keV}$.

[19] See e.g. ref. [37] for the details of energy scale calibration of the liquid Xe detectors.

[20] For $E_d = 0\,\mathrm{kV/cm}$, $S_e = S_n = 1$.

JHEP03(2018)194

In the presence of the transition due to the Migdal effect, the nuclear recoil is accompanied by electronic energy injections in the sub-keV to the keV range. By ignoring the energy resolution of the detectors, the electron equivalent energy spectrum is given by

$$\frac{dR}{dE_{\rm det}dv_{DM}} \simeq \int dE_R dE_{EM}\, \delta(E_{\rm det} - q_{nr}E_R - E_{EM}) \frac{dR}{dE_R\, dE_{EM}\, dv_{DM}}\,, \tag{6.2}$$

with q_{nr} being the conversion between E_{nr} and E_{ee} in eq. (6.1) (see also eqs. (4.24) and (4.25)). In the following, we include only the electronic energy injection caused by the ionizations as the excitation probabilities into the unoccupied binding energy levels are much smaller than the ionization probabilities.[21]

In figure 5, we show the total electron equivalent energy spectrum for a given spin-independent scattering cross section of dark matter on nucleons through the contact interaction.[22] Here, we assume a detector with $E_d = 0\,{\rm kV/cm}$ as in the single-phase experiment such as the XMASS experiment [48]. We also fix $q_{nr} = \mathcal{L}_{\rm eff} = 0.15$. We adopt the Helm form factor [5, 8]. The local dark matter density is fixed to a conventional value, $\rho_{DM} = 0.3\,{\rm GeV/cm^3}$. The local circular velocity is also fixed to be $v_{\rm circ} = 220\,{\rm km/s}$ with the peculiar motions of the Earth neglected.[23] We also assume a Maxwell velocity distribution with the velocity dispersion, $v_0 = 220\,{\rm km/s}$, which is truncated at the Galactic escape velocity $v_{\rm esc} = 544\,{\rm km/s}$.

The figures show that the electronic energy from the ionizations can be larger than the maximum value of the (electron equivalent) nuclear recoil energy for a rather light dark matter. As discussed in the previous section, the shape of the energy spectrum of the electronic injections is not sensitive to the incident dark matter velocity as long as they are kinematically allowed. The nuclear recoil energy, on the other hand, depends on the dark matter velocity,

$$E_R \simeq \frac{q_A^2}{2m_A} \lesssim \frac{1}{2}\frac{\mu_N^2}{m_A} v_{DM}^2\,, \tag{6.3}$$

which is suppressed for light dark matter. These features can be seen from the figures; the electronic energy from the ionizations are less sensitive to the dark matter mass, while the maximum nuclear recoil energy is sensitive.

Given a typical threshold of the electron equivalent energy of the liquid Xe detectors of about a ${\rm keV}_{ee}$, the ionization from $n = 3$ provides a new detection channel for rather light dark matter. For example, with exposures of about $10^5\,{\rm kg{\cdot}days}$, a few hundred events are expected for $m_{DM} \simeq 500\,{\rm MeV}$ and $\bar{\sigma}_n \simeq 10^{-36}{\rm cm}^2$ in the liquid Xe detectors.[24] Similarly, a few signal events are expected for $m_{DM} \simeq 5\,{\rm GeV}$ for $\bar{\sigma}_n \simeq 10^{-42}{\rm cm}^2$ for the same exposure. It should be noted that those signals are eliminated as background events in

[21] Moreover, the excitation into the unoccupied binding energy levels are not well defined when the electronic band structure is formed in the medium.

[22] The nucleon-dark matter cross section $\bar{\sigma}_n$ is related to $\bar{\sigma}_N$ via, $\bar{\sigma}_N = A^2 \times \mu_N^2/\mu_n^2 \times \bar{\sigma}_n$ for $g_p = p_n$.

[23] The annual modulation caused by the Earth's peculiar motion can be significantly enhanced as of the inelastic nuclear scattering [49].

[24] For much lighter dark matter, the ionizations from $n_I = 3$ require very fast dark matter (see figure 1), and hence, the event rate is highly suppressed due to the dark matter velocity distribution.

JHEP03(2018)194

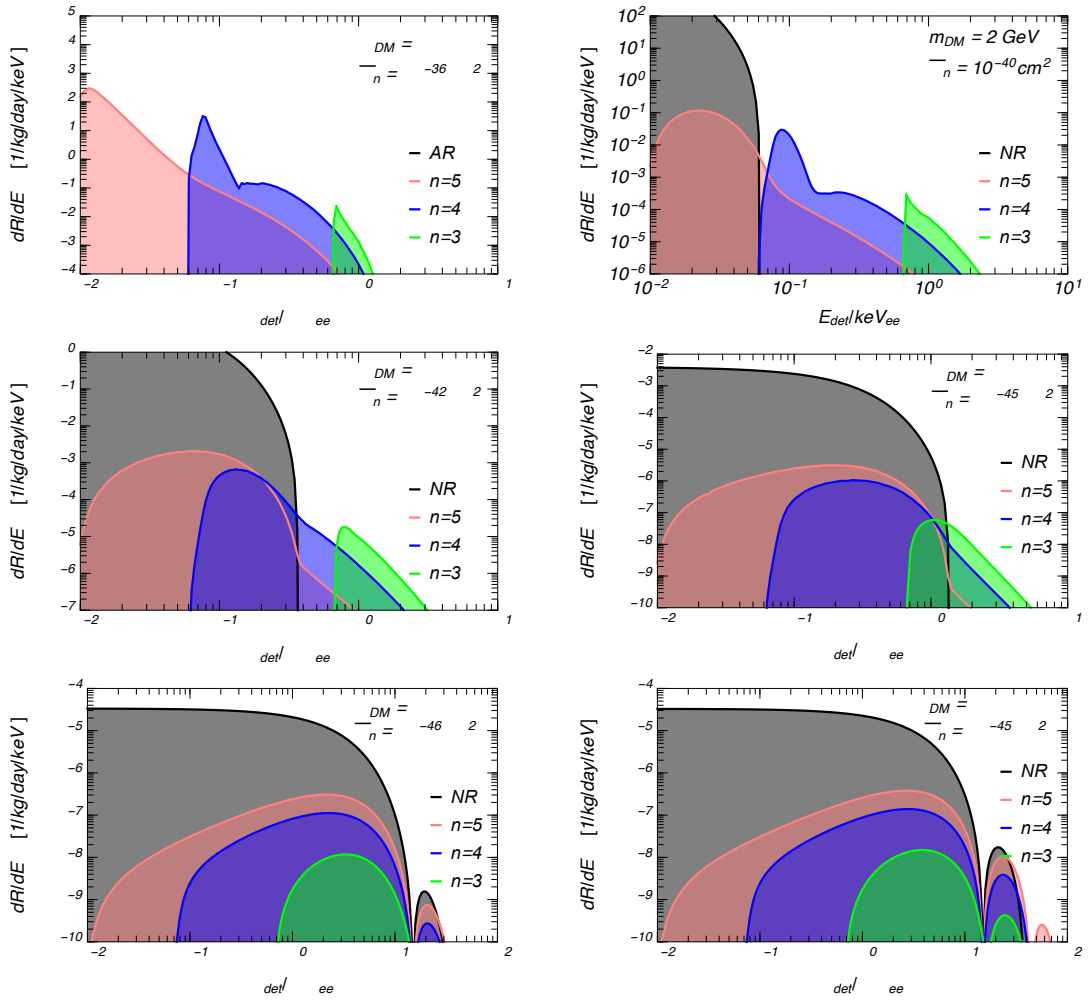

Figure 5. The differential event rates expected at the single-phase experiments with the liquid Xe target. The black lines show the nuclear recoil (NR) spectrum without ionization. (The NR spectrum with respect to $E_{\rm det}$ and the one with respect to E_R differ by a factor of $1/q_{nr}$.) The green, blue, and pink lines show the ionization rates from $n = 3, 4$, and 5, respectively. Here, we do not take the energy resolution into account. Since we apply the estimations for the isolated atoms, the ionization spectrum from the valence electrons, i.e. $n = 5$, are not reliable.

the conventional analysis of the dual-phase experiments. In those experiments, one needs different analyses to cover such signals (see e.g. [50, 51]).

For heavier dark matter, $m_{DM} > \mathcal{O}(10)\,\text{GeV}$, on the other hand, the Migdal effect is submerged below the conventional nuclear recoil spectrum, and hence, does not affect the detector sensitivities. In principle, the additional electronic energy injections affect the so-called S2/S1 ratio in the dual-phase detectors. This is because the numbers of direct excitons N_{ex} and direct ionizations N_i are different for the atomic recoil and the electronic recoil.[25] However, such effects should have been taken into account by the detector calibration by the neutron sources for a given momentum transfer.

[25]For the electronic recoil, the ratio is given by $N_{ex}/N_i \simeq 0.06$ [52], while it is $N_{ex}/N_i \sim 1$ [37, 40] for the atomic recoil.

JHEP03(2018)194

Finally, let us compare the Migdal effect with the Bremsstrahlung of the nucleus [53] (see also [54]). Similarly to the Migdal effect, the Bremsstrahlung is also a universal effect and irreducible. The expected rates are, however, suppressed by the mass of the nucleus, E_R/m_N, and hence, they are much smaller than the ones of the Migdal effect for E_R in the keV range. The Migdal effect should also be distinguished from the photon emissions in the inelastic nuclear scatterings which require a larger momentum transfer [24, 25].

7 Migdal effects in coherent neutrino-nucleus scattering

As another application, let us briefly discuss the Migdal effects in the coherent neutrino-nucleus scattering (CνNS). In a similar manner to the dark matter scattering cross section, the differential cross section of the coherent neutrino-nucleus scattering with the Migdal effect is given by

$$\frac{d\sigma}{dE_R} \simeq \sum_{E_{ec}^F} \frac{d\sigma_{C\nu NS}}{dE_R} \times |Z_{FI}(q_e)|^2 \,. \tag{7.1}$$

Here, $\sigma_{C\nu NS}$ denotes the coherent neutrino-nucleus scattering [55–57],

$$\frac{d\sigma_{C\nu NS}}{dE_R} = \frac{|F_A(q_A^2)|^2 Q_W^2 G_F^2 m_A}{8\pi} \left(1 - \frac{m_A E_R}{2E_\nu^2}\right), \tag{7.2}$$

with G_F, $\sin\theta_W$, N, Q_W being the Fermi constant, the weak mixing angle, the number of neutrons $N = A - Z$, and the weak charge of the nucleus $Q_W = N - (1 - 4\sin^2\theta_W)Z \simeq N$, respectively. As in the previous section, the magnetic quantum numbers of the electrons in the initial/final states are averaged/summed. For given E_ν and ΔE, the recoil energy is constrained in

$$\frac{\Delta E^2}{2m_A} < E_R < \frac{(2E_\nu - \Delta E)^2}{2(m_A + 2E_\nu)}, \tag{7.3}$$

where the maximal recoil energy corresponds to the back-to-back scattering.

In figure 6, we show the total electron equivalent energy spectra for the CνNS for the pp and the ^{8}B solar neutrinos. Here, we take the central values of the neutrino fluxes of the SFII-GS98 model given in ref. [58]. The single-phase liquid Xe detectors are assumed as in the previous section with $q_{nr} = 0.15$. The figures show that the nuclear recoil signal without the Migdal effect is below the energy thresholds of the current liquid Xe detectors, i.e. $\mathcal{O}(1)$ keV. The signal of the ionization from $n_I = 3$ is, on the other hand, above the energy threshold, a few events of which are expected with exposures of about 10 ton·years.[26]

8 Conclusions and discussion

In this paper, we reformulated the Migdal effect at the nuclear recoil caused by a dark matter scattering and a coherent neutrino-nuclear scattering. In our formalism, we take the

[26] More detailed study including background estimation will be given elsewhere.

JHEP03(2018)194

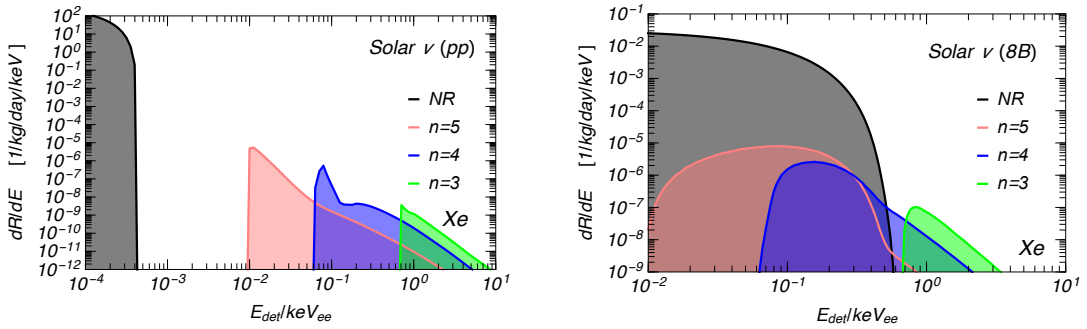

Figure 6. The differential event rates for expected for the coherent neutrino-nucleus scattering for the pp and the ^{8}B solar neutrinos. The single-phase liquid Xe detectors are assumed as in the previous section with $q_{nr} = 0.15$. The black lines show the nuclear recoil (NR) spectrum without the ionizations. (The NR spectrum with respect to $E_{\rm det}$ and the one with respect to E_R differ by a factor of $1/q_{nr}$.) Since we apply the estimations for the isolated atoms, the ionization spectrum from the valence electrons are not reliable.

plane waves of the whole atomic system as the asymptotic states for the scattering process. The coherent treatment of the electron cloud makes the energy-momentum conservation and the probability conservation transparent. We also provide numerical estimates of the ionization and the excitation rates for isolated atoms of Ar, Xe, Ge, Na, and I by using the `Flexible Atomic Code (FAC, cFAC)` [32].

We also applied the results for the dark matter direct detections by taking a liquid Xe detector as an example. We showed that the ionization signals through the Migdal effect provide new detection channels for light dark matter with a mass in the GeV range. Since such signals are eliminated as background events in the conventional analysis of the dual-phase experiments, different analyses are required to cover such signals. For rather heavy dark matter, on the other hand, the Migdal effects are submerged below the conventional atomic recoil spectrum.

In our analysis, we have not studied detailed detector responses nor the precise treatment of the Migdal effects of the non-isolated atoms in liquid or crystals. For more precise estimation, detailed detector simulations are imperative. In particular, it is important to study detector responses to the energy released by the de-excitation of the core-hole. More theoretical efforts are also required for precise estimation of the Migdal effect in the medium.

We also note that it is an interesting future work to discuss whether the Migdal effect affects the direct detection experiments that mainly aim the electron recoil [59–67]. As the Migdal effect provides the electronic signals via the nuclear recoil, dark matter without electron recoil can be searched for by those experiments.

Acknowledgments

The authors acknowledge Y. Itow, Y. Kishimoto, and S. Moriyama for useful discussion. The authors also acknowledge H. Ejiri for his informative seminar at ICRR, which drew our attention to the Migdal effect. This work is supported in part by Grants-in-Aid for Scientific Research from the Ministry of Education, Culture, Sports, Science, and Technology (MEXT) KAKENHI, Japan, No. 25105011, No. 15H05889 and No. 17H02878 (M.I.).

JHEP03(2018)194

A The normalization of the projection operator

In this appendix, we show that the total projection operator is given by

$$\int d\hat{P} = \int \frac{d^3\mathbf{p}_A}{(2\pi)^3} \sum_{E_{ec}^F} |\Psi_E\rangle\langle\Psi_E| = \mathbb{1}\,, \tag{A.1}$$

where the summation is taken for all the possible electron cloud configurations including the continuous spectrum. In terms of the one-electron states, the projection operators can also be written by

$$\int d\hat{P} = \int \frac{d^3\mathbf{p}_A}{(2\pi)^3} \left(|\mathbf{p}_N\rangle\langle\mathbf{p}_N|\right) \left(\prod_{i=1}^{N_e} \sum\!\!\!\!\!\!\int_{o_i} |\tilde{\phi}_{o_i}\rangle\langle\tilde{\phi}_{o_i}| \right) = \mathbb{1}\,, \tag{A.2}$$

where

$$|\mathbf{p}_N\rangle = \int d^3\mathbf{x}_N\, |\mathbf{x}_N\rangle\, e^{i\mathbf{p}_N\cdot\mathbf{x}_N}\,, \tag{A.3}$$

$$|\tilde{\phi}_{o_i}\rangle = e^{i\mathbf{q}_e\cdot\mathbf{x}_i - i\hat{\mathbf{x}}_N\cdot\hat{\mathbf{p}}_i}|\phi_{o_i}\rangle\,, \tag{A.4}$$

$$\mathbf{p}_N = m_N\mathbf{v} = \frac{m_N}{\overline{m}_A}\mathbf{p}_A\,, \tag{A.5}$$

$$\mathbf{q}_e = m_e\mathbf{v} = \frac{m_e}{\overline{m}_A}\mathbf{p}_A\,, \tag{A.6}$$

$$\sum\!\!\!\!\!\!\int_{o_i} = \sum_{n_i,\kappa_i,m_i} + \sum_{\kappa_i,m_i}\int \frac{dE_i}{2\pi}\,. \tag{A.7}$$

Here, $|\phi_{o_i}\rangle$ denotes the energy eigenstate for a single orbital which corresponds to

$$\langle\mathbf{x}_i,\alpha_i|\phi_{o_i}\rangle = \phi_{o_i}^{\alpha_i}(\mathbf{x}_i)\,, \tag{A.8}$$

in the coordinate representations with the spinor index α_i. The one particle states are normalized such that

$$\langle\phi_o|\phi_{o'}\rangle = \delta_{nn'}\delta_{\kappa\kappa'}\delta_{mm'}\ (E_o<0)\,, \tag{A.9}$$

$$\langle\phi_o|\phi_{o'}\rangle = (2\pi)\delta(E_o-E'_o)\delta_{\kappa\kappa'}\delta_{mm'}\ (E_o>0)\,, \tag{A.10}$$

$$\langle\mathbf{p}_N|\mathbf{p}'_N\rangle = (2\pi)\delta^3(\mathbf{p}_N-\mathbf{p}'_N)\,. \tag{A.11}$$

In this notation, the energy eigenstate in eq. (2.21) is given by

$$|\Psi_E\rangle = \left(\sum_{\sigma\in S_{N_e}} \frac{\mathrm{sgn}(\sigma)}{\sqrt{N_e!}} \Pi_{i=1}^{N_e} e^{i\mathbf{q}_e\cdot\hat{\mathbf{x}}_i - i\hat{\mathbf{x}}_N\cdot\hat{\mathbf{p}}_i}|\phi_{o_{\sigma(i)}}\rangle \right)|\mathbf{p}_N\rangle\,. \tag{A.12}$$

By applying the operator in eq. (A.2) on eq. (A.12), we obtain,

$$\begin{aligned}\int d\hat{P}|\Psi_E\rangle = \int \frac{d^3\mathbf{p}'_A}{(2\pi)^3}|\mathbf{p}'_N\rangle \\ \times \langle\mathbf{p}'_N|\left(\sum_{\sigma\in S_{N_e}} \frac{\mathrm{sgn}(\sigma)}{\sqrt{N_e!}} \Pi_{i=1}^{N_e} \sum\!\!\!\!\!\!\int_{o_i} |\tilde{\phi}_{o_i}\rangle\langle\tilde{\phi}_{o_i}|e^{i\mathbf{q}_e\cdot\hat{\mathbf{x}}_i - i\hat{\mathbf{x}}_N\cdot\hat{\mathbf{p}}_i}|\phi_{o_{\sigma(i)}}\rangle \right)|\mathbf{p}_N\rangle\,.\end{aligned} \tag{A.13}$$

JHEP03(2018)194

By inserting the projection operator,

$$\mathbb{1} = \int d^3\mathbf{x}_N |\mathbf{x}_N\rangle\langle\mathbf{x}_N| \times \prod_{i=1}^{N_e} d^3\mathbf{x}_i \sum_{\alpha_i} |\mathbf{x}_i, \alpha_i\rangle\langle\mathbf{x}_i, \alpha_i| \,, \tag{A.14}$$

eq. (A.13) is reduced to

$$\begin{aligned}
&\int \frac{d^3\mathbf{p}'_A}{(2\pi)^3} |\mathbf{p}'_N\rangle d^3\mathbf{x}_N e^{-i(\mathbf{p}'_N - \mathbf{p}_N)\cdot\mathbf{x}_N} \\
&\quad \times \left(\sum_{\sigma\in S_{N_e}} \frac{\mathrm{sgn}(\sigma)}{\sqrt{N_e!}} \Pi_{i=1}^{N_e} \sum\!\!\!\!\!\!\int_{o_i} |\tilde{\phi}_{o_i}\rangle d^3\mathbf{x}_i \sum_{\alpha_i} e^{-i(\mathbf{q}_e{}' - \mathbf{q}_e)\cdot\mathbf{x}_i} \phi_{o_i}^{\alpha_i *}(\mathbf{x}_i - \mathbf{x}_N) \phi_{o_{\sigma(i)}}^{\alpha_i}(\mathbf{x}_i - \mathbf{x}_N) \right) \\
&= \int \frac{d^3\mathbf{p}'_A}{(2\pi)^3} |\mathbf{p}'_N\rangle d^3\mathbf{x}_N e^{-i((\mathbf{p}'_N + N_e\mathbf{q}_e{}') - (\mathbf{p}_N + N_e\mathbf{q}_e))\cdot\mathbf{x}_N} \\
&\quad \times \left(\sum_{\sigma\in S_{N_e}} \frac{\mathrm{sgn}(\sigma)}{\sqrt{N_e!}} \Pi_{i=1}^{N_e} \sum\!\!\!\!\!\!\int_{o_i} |\tilde{\phi}_{o_i}\rangle d^3\mathbf{x}_i \sum_{\alpha_i} e^{-i(\mathbf{q}_e{}' - \mathbf{q}_e)\cdot\mathbf{x}_i} \phi_{o_i}^{\alpha_i *}(\mathbf{x}_i) \phi_{o_{\sigma(i)}}^{\alpha_i}(\mathbf{x}_i) \right) ,
\end{aligned} \tag{A.15}$$

where we have shifted the integration variable $\mathbf{x}_i$ by $\mathbf{x}_N$. By remembering

$$\mathbf{p}_N + N_e\mathbf{q}_e = \mathbf{p}_A \,, \tag{A.16}$$

we find

$$\begin{aligned}
&\int d^3\mathbf{p}'_A |\mathbf{p}'_N\rangle \delta^3(\mathbf{p}'_A - \mathbf{p}_A) \\
&\quad \times \left(\sum_{\sigma\in S_{N_e}} \frac{\mathrm{sgn}(\sigma)}{\sqrt{N_e!}} \Pi_{i=1}^{N_e} \sum\!\!\!\!\!\!\int_{o_i} |\tilde{\phi}_{o_i}\rangle d^3\mathbf{x}_i \sum_{\alpha_i} \phi_{o_i}^{\alpha_i *}(\mathbf{x}_i) \phi_{o_{\sigma(i)}}^{\alpha_i}(\mathbf{x}_i) \right) ,
\end{aligned} \tag{A.17}$$

where we have used $\mathbf{q}_e{}' = \mathbf{q}_e$ for $\mathbf{p}'_A = \mathbf{p}_A$. Finally, by using the orthogonality of the electron orbitals, we confirm that

$$\int d\hat{P} |\Psi_E\rangle = |\Psi_E\rangle \,. \tag{A.18}$$

B Probability conservation and occupied-occupied transition

Let us discuss the probability conservation,

$$\sum_{E_{ec}^F} |Z_{FI}(\mathbf{q}_e)|^2 = 1 \,, \tag{B.1}$$

in terms of the single electron transition amplitudes. As discussed in section 4.1, the electron excitation/ionization amplitude is reduced to

$$\langle \Phi_{E_{ec}^F} | e^{-i\sum \mathbf{q}_e\cdot\hat{\mathbf{x}}_i} | \Phi_{E_{ec}^I} \rangle \simeq -i\langle \phi_{o'_k} | i\mathbf{q}_e \cdot \hat{\mathbf{x}} | \phi_{o_k} \rangle \,, \tag{B.2}$$

JHEP03(2018)194

at the leading order of q_e. Here we use the notation in the appendix A. Accordingly, the excitation probability is given by

$$\mathcal{P}_{\rm ex} = \sum_{E^F_{ec}} |\langle \Phi_{E^F_{ec}} | e^{-i\sum \mathbf{q}_e\cdot\hat{\mathbf{x}}_i} | \Phi_{E^I_{ec}} \rangle|^2 \simeq \sum_{k=1}^{N_e} \sum_{o\notin ec_I} |\langle \phi_o | i\mathbf{q}_e\cdot\hat{\mathbf{x}} | \phi_{o_k}\rangle|^2 \,. \tag{B.3}$$

The forward amplitude is, on the other hand, given by

$$\langle \Phi_{E^I_{ec}} | e^{-i\sum \mathbf{q}_e\cdot\hat{\mathbf{x}}_i} | \Phi_{E^I_{ec}} \rangle \simeq 1 - \frac{1}{2}\sum_{i=1}^{N_e} \langle \phi_{o_i} | (\mathbf{q}_e\cdot\hat{\mathbf{x}})^2 | \phi_{o_i}\rangle + \frac{1}{2}\sum_{i,j=1\,(i\neq j)}^{N_e} \left| \langle \phi_{o_i} | \mathbf{q}_e\cdot\hat{\mathbf{x}} | \phi_{o_j}\rangle \right|^2 , \tag{B.4}$$

which leads to the probability with the electron cloud unchanged,

$$\mathcal{P}_{\rm unchanged} \simeq 1 - \sum_{i=1}^{N_e} \langle \phi_{o_i} | (\mathbf{q}_e\cdot\hat{\mathbf{x}})^2 | \phi_{o_i}\rangle + \sum_{k=1}^{N_e} \sum_{o\in ec_I\setminus\{o_k\}} |\langle \phi_o | \mathbf{q}_e\cdot\hat{\mathbf{x}} | \phi_{o_k}\rangle|^2 \,. \tag{B.5}$$

Let us define probabilities of the single electron transitions,

$$p_{\rm unchanged}(k) = \left| \langle \phi_{o_k} | e^{i\mathbf{q}_e\cdot\hat{\mathbf{x}}} | \phi_{o_k}\rangle \right|^2 \simeq \left| 1 - \frac{1}{2}\langle \phi_{o_k} | (\mathbf{q}_e\cdot\hat{\mathbf{x}})^2 | \phi_{o_k}\rangle \right|^2 , \tag{B.6}$$

$$p_{\rm ex}(k) = \sum_{o\notin ec_I} \left| \langle \phi_o | e^{i\mathbf{q}_e\cdot\hat{\mathbf{x}}} | \phi_{o_k}\rangle \right|^2 \simeq \sum_{o\notin ec_I} |\langle \phi_o | \mathbf{q}_e\cdot\hat{\mathbf{x}} | \phi_{o_k}\rangle|^2 , \tag{B.7}$$

$$p_{\rm occupied}(k) = \sum_{o\in ec_I\setminus\{o_k\}} \left| \langle \phi_o | e^{i\mathbf{q}_e\cdot\hat{\mathbf{x}}} | \phi_{o_k}\rangle \right|^2 \simeq \sum_{o\in ec_I\setminus\{o_k\}} |\langle \phi_o | \mathbf{q}_e\cdot\hat{\mathbf{x}} | \phi_{o_k}\rangle|^2 , \tag{B.8}$$

up to $\mathcal{O}(q_e^3)$. The probability $p_{\rm occupied}(k)$ denotes the transition between the occupied orbitals. The single electron transition probabilities satisfy

$$p_{\rm unchanged}(k) + p_{\rm ex}(k) + p_{\rm occupied}(k) \simeq \sum_o \left| \langle \phi_o | e^{i\mathbf{q}_e\cdot\hat{\mathbf{x}}} | \phi_{o_k}\rangle \right|^2 = 1 \,. \tag{B.9}$$

To the order of $\mathcal{O}(q_e^2)$, the total probabilities can be expressed by using the single electron transition probabilities,

$$\mathcal{P}_{\rm unchanged} + \mathcal{P}_{\rm ex} \simeq \prod_i \left(p_{\rm unchanged}(k) + p_{\rm ex}(k) + p_{\rm occupied}(k) \right) . \tag{B.10}$$

Thus, we find that eq. (B.9) guarantees the probability conservation in terms of the single electron transition probabilities. It should be emphasized that $p_{\rm occupied}$ plays an important role for the conservation of the probability. As is clear from the above argument, however, $p_{\rm occupied}$ is a part of $\mathcal{P}_{\rm unchanged}$, and hence, it does not contribute to $\mathcal{P}_{\rm ex}$ up to $\mathcal{O}(q_e^3)$.

C Dirac-Hartree-Fock method

In this appendix, we briefly review the Dirac-Hartree-Fock method in the natural units (see [28, 32] for review). The Hamiltonian for the electrons is given by

$$\hat{H}_{ec} = \sum_j \hat{h}_j + \sum_{i<j} \frac{\alpha}{|\hat{\mathbf{r}}_i - \hat{\mathbf{r}}_j|} \,, \tag{C.1}$$

JHEP03(2018)194

where

$$\hat{h}_j = \bar{\boldsymbol{\alpha}} \cdot \mathbf{p}_j + m_e(\beta - 1) + V_N(|\hat{\mathbf{r}}_j|)\,. \tag{C.2}$$

Here, we ignore the Breit interaction terms and

$$V_N(r) = \begin{cases} -\frac{Z\alpha}{2R_N}\left[3 - \left(\frac{r}{R_N}\right)^2\right], & r \le R_N \\ -\frac{Z\alpha}{r}, & r > R_N \end{cases}, \tag{C.3}$$

with $\alpha m_e R_N = 2.2677 \times 10^{-5} A^{1/3}$. The Dirac matrices $\bar{\boldsymbol{\alpha}}$ and β are defined by

$$\bar{\boldsymbol{\alpha}} = \begin{pmatrix} 0 & \boldsymbol{\sigma} \\ \boldsymbol{\sigma} & 0 \end{pmatrix}, \quad \beta = \begin{pmatrix} 1_2 & 0 \\ 0 & -1_2 \end{pmatrix}, \tag{C.4}$$

where $\boldsymbol{\sigma} = (\sigma_1, \sigma_2, \sigma_3)$ are the Pauli matrices.

We assume that the electron wave function for the ground state is approximately given by

$$\Phi(\mathbf{r}_1, \cdots, \mathbf{r}_N) = \sum_{\sigma \in S_N} \frac{\mathrm{sgn}(\sigma)}{\sqrt{N!}} \prod_{j=1}^{N} \phi_{o_{\sigma(j)}}(\mathbf{r}_j)\,, \tag{C.5}$$

with

$$\phi_{o=\{E_{n\kappa},\kappa,m\}}(\mathbf{r}) = \frac{1}{r}\begin{pmatrix} P_{n\kappa}(r)\Omega_{\kappa m}(\theta,\varphi) \\ iQ_{n\kappa}(r)\Omega_{-\kappa m}(\theta,\varphi) \end{pmatrix}. \tag{C.6}$$

Here we use n and κ, instead of E, to label the radial wave functions. We choose $\{o_i\}$ to be one of the ground state configurations.[27]

The ground state wave functions are determined by the variational method. The expectation value of the Hamiltonian is calculated as

$$\begin{aligned} \langle\Phi|\hat{H}_{ec}|\Phi\rangle = &\sum_j \langle\phi_{o_j}|\hat{h}|\phi_{o_j}\rangle + \sum_{i<j}\langle\phi_{o_i},\phi_{o_j}|\frac{\alpha}{|\hat{\mathbf{r}}_0 - \hat{\mathbf{r}}'_0|}|\phi_{o_i},\phi_{o_j}\rangle \\ &- \sum_{i<j}\langle\phi_{o_j},\phi_{o_i}|\frac{\alpha}{|\hat{\mathbf{r}}_0 - \hat{\mathbf{r}}'_0|}|\phi_{o_i},\phi_{o_j}\rangle\,, \end{aligned} \tag{C.7}$$

where h is the same as h_j but operates on a single electron state. Here, the expectation values in the coordinate representation are give by

$$\langle\Phi'|\Phi\rangle \equiv \sum_{\sigma',\sigma} \frac{\mathrm{sgn}(\sigma')\mathrm{sgn}(\sigma)}{N!} \prod_{j=1}^{N} \langle\phi_{o'_{\sigma'(j)}})|\phi_{o_{\sigma(j)}}\rangle\,, \tag{C.8}$$

$$\langle\phi_{o'}|f(\hat{\mathbf{r}}_0)|\phi_o\rangle \equiv \sum_\alpha \int d^3\mathbf{r}_0 [\phi^\alpha_{o'}(\mathbf{r}_0)]^* \phi^\alpha_o(\mathbf{r}_0) f(\mathbf{r}_0)\,, \tag{C.9}$$

$$\langle\phi_{o_1},\phi_{o_2}|f(\hat{\mathbf{r}}_0,\hat{\mathbf{r}}'_0)|\phi_{o_3},\phi_{o_4}\rangle \equiv \sum_{\alpha,\beta} \int d^3\mathbf{r}_0 d^3\mathbf{r}'_0 [\phi^\alpha_{o_1}(\mathbf{r})\phi^\beta_{o_2}(\mathbf{r}'_0)]^* \phi^\alpha_{o_3}(\mathbf{r}_0)\phi^\beta_{o_4}(\mathbf{r}'_0) f(\mathbf{r}_0,\mathbf{r}'_0)\,. \tag{C.10}$$

[27] In `FAC`, a fictitious mean configuration with fractional occupation numbers is used if there are more than one ground state configurations.

JHEP03(2018)194

By taking the variation for the coordinate of one of the orbital electrons, we obtain

$$0 = \hat{h}\phi_{o_j}(\mathbf{r}) + \left[\sum_{i(i\neq j)} \langle\phi_{o_i}|\frac{\alpha}{|\mathbf{r}-\hat{\mathbf{r}}_0|}|\phi_{o_i}\rangle\right]\phi_{o_j}(\mathbf{r}) - \left[\sum_{i(i\neq j)} \phi_{o_i}(\mathbf{r})\langle\phi_{o_i}|\frac{\alpha}{|\mathbf{r}-\hat{\mathbf{r}}_0|}\right]|\phi_{o_j}\rangle - \varepsilon_{o_j}\phi_{o_j}(\mathbf{r}) + h.c.\,, \tag{C.11}$$

where ε_o is a Lagrange multiplier to impose

$$\langle\Phi|\Phi\rangle = 1\,. \tag{C.12}$$

This is the so-called Dirac-Hartree-Fock equation and gives simultaneous differential equations for ϕ_{o_j}. The second and the third terms express the electron-electron interaction and can be seen as local and non-local potentials for ϕ_{o_j}, respectively, once ϕ_{o_i} are treated as mean fields.

Since the non-local potential is numerically demanding, the Slater approximation is often adopted to localize the potential [68, 69]. However, since it has incorrect asymptotic behavior, `FAC` uses an improved potential given in eq. (5.2). From eq. (C.11), we finally obtain,

$$\left(\frac{d}{dr} + \frac{\kappa}{r}\right) P_{n\kappa}(r) = \left(\varepsilon_{n\kappa} - V(r) + 2m_e\right) Q_{n\kappa}(r)\,, \tag{C.13}$$

$$\left(\frac{d}{dr} - \frac{\kappa}{r}\right) Q_{n\kappa}(r) = \left(-\varepsilon_{n\kappa} + V(r)\right) P_{n\kappa}(r)\,, \tag{C.14}$$

with

$$V(r) = V_N(r) + V_{ee}(r)\,, \tag{C.15}$$

which is solved iteratively for the ground state. As for the excited states and the unbouded states, the single electron wave functions are obtained by solving eqs. (C.13) and (C.14) by using the potential in eq. (5.2), which is iteratively obtained for the ground state.

References

[1] G. Bertone, D. Hooper and J. Silk, *Particle dark matter: Evidence, candidates and constraints*, *Phys. Rept.* **405** (2005) 279 [hep-ph/0404175] [INSPIRE].

[2] H. Murayama, *Physics Beyond the Standard Model and Dark Matter*, in *Les Houches Summer School — Session 86: Particle Physics and Cosmology: The Fabric of Spacetime*, Les Houches, France, July 31–August 25, 2006 (2007), arXiv:0704.2276 [INSPIRE].

[3] J.L. Feng, *Dark Matter Candidates from Particle Physics and Methods of Detection*, *Ann. Rev. Astron. Astrophys.* **48** (2010) 495 [arXiv:1003.0904] [INSPIRE].

JHEP03(2018)194

[4] B.W. Lee and S. Weinberg, *Cosmological Lower Bound on Heavy Neutrino Masses*, *Phys. Rev. Lett.* **39** (1977) 165 [INSPIRE].

[5] G. Jungman, M. Kamionkowski and K. Griest, *Supersymmetric dark matter*, *Phys. Rept.* **267** (1996) 195 [hep-ph/9506380] [INSPIRE].

[6] M.W. Goodman and E. Witten, *Detectability of Certain Dark Matter Candidates*, *Phys. Rev.* **D 31** (1985) 3059 [INSPIRE].

[7] F. Nesti and P. Salucci, *The Dark Matter halo of the Milky Way, AD 2013*, *JCAP* **07** (2013) 016 [arXiv:1304.5127] [INSPIRE].

[8] J.D. Lewin and P.F. Smith, *Review of mathematics, numerical factors and corrections for dark matter experiments based on elastic nuclear recoil*, *Astropart. Phys.* **6** (1996) 87 [INSPIRE].

[9] R.J. Gaitskell, *Direct detection of dark matter*, *Ann. Rev. Nucl. Part. Sci.* **54** (2004) 315.

[10] T. Marrodán Undagoitia and L. Rauch, *Dark matter direct-detection experiments*, *J. Phys.* **G 43** (2016) 013001 [arXiv:1509.08767] [INSPIRE].

[11] LUX collaboration, D.S. Akerib et al., *Results from a search for dark matter in the complete LUX exposure*, *Phys. Rev. Lett.* **118** (2017) 021303 [arXiv:1608.07648] [INSPIRE].

[12] PandaX-II collaboration, A. Tan et al., *Dark Matter Results from First 98.7 Days of Data from the PandaX-II Experiment*, *Phys. Rev. Lett.* **117** (2016) 121303 [arXiv:1607.07400] [INSPIRE].

[13] XENON collaboration, E. Aprile et al., *First Dark Matter Search Results from the XENON1T Experiment*, *Phys. Rev. Lett.* **119** (2017) 181301 [arXiv:1705.06655] [INSPIRE].

[14] J.D. Vergados and H. Ejiri, *The role of ionization electrons in direct neutralino detection*, *Phys. Lett.* **B 606** (2005) 313 [hep-ph/0401151] [INSPIRE].

[15] C.C. Moustakidis, J.D. Vergados and H. Ejiri, *Direct dark matter detection by observing electrons produced in neutralino-nucleus collisions*, *Nucl. Phys.* **B 727** (2005) 406 [hep-ph/0507123] [INSPIRE].

[16] H. Ejiri, C.C. Moustakidis and J.D. Vergados, *Dark matter search by exclusive studies of X-rays following WIMPs nuclear interactions*, *Phys. Lett.* **B 639** (2006) 218 [hep-ph/0510042] [INSPIRE].

[17] J.D. Vergados, H. Ejiri and K.G. Savvidy, *Theoretical direct WIMP detection rates for inelastic scattering to excited states*, *Nucl. Phys.* **B 877** (2013) 36 [arXiv:1307.4713] [INSPIRE].

[18] R. Bernabei et al., *On electromagnetic contributions in WIMP quests*, *Int. J. Mod. Phys.* **A 22** (2007) 3155 [arXiv:0706.1421] [INSPIRE].

[19] B.M. Roberts, V.V. Flambaum and G.F. Gribakin, *Ionization of atoms by slow heavy particles, including dark matter*, *Phys. Rev. Lett.* **116** (2016) 023201 [arXiv:1509.09044] [INSPIRE].

[20] B.M. Roberts, V.A. Dzuba, V.V. Flambaum, M. Pospelov and Y.V. Stadnik, *Dark matter scattering on electrons: Accurate calculations of atomic excitations and implications for the DAMA signal*, *Phys. Rev.* **D 93** (2016) 115037 [arXiv:1604.04559] [INSPIRE].

[21] A.B. Migdal, *Ionization of atoms accompanying α- and β-decay*, *J. Phys. USSR* **4** (1941) 449.

JHEP03(2018)194

[22] G. Baur, F. Rosel and D. Trautmann, *Ionisation induced by neutrons*, *J. Phys.* **B 16** (1983) L419.

[23] L.D. Landau and E.M. Lifshits, *Quantum Mechanics*, in *Course of Theoretical Physics*, Vol. 3, Butterworth-Heinemann, Oxford (1991).

[24] J.R. Ellis, R.A. Flores and J.D. Lewin, *Rates for Inelastic Nuclear Excitation by Dark Matter Particles*, *Phys. Lett.* **B 212** (1988) 375 [INSPIRE].

[25] R. Bernabei et al., *Improved limits on WIMP-^{129}Xe inelastic scattering*, *New J. Phys.* **2** (2000) 15.

[26] C. McCabe, *The Astrophysical Uncertainties Of Dark Matter Direct Detection Experiments*, *Phys. Rev.* **D 82** (2010) 023530 [arXiv:1005.0579] [INSPIRE].

[27] A.M. Green, *Astrophysical uncertainties on direct detection experiments*, *Mod. Phys. Lett.* **A 27** (2012) 1230004 [arXiv:1112.0524] [INSPIRE].

[28] W.R. Johnson, *Atomic Structure Theory: Lectures on Atomic Physics*, Springer (2007).

[29] W. Bambynek et al., *X-Ray Fluorescence Yields, Auger and Coster-Kronig Transition Probabilities*, *Rev. Mod. Phys.* **44** (1972) 716 [*Erratum ibid.* **46** (1974) 853] [INSPIRE].

[30] J. Campbell and T. PAPP, *Widths of the atomic K-N7 levels*, *Atom. Data Nucl. Data tables* **77** (2001) 1.

[31] S.-K. Son and R. Santra, *Monte Carlo calculation of ion, electron, and photon spectra of xenon atoms in x-ray free-electron laser pulses*, *Phys. Rev.* **A 85** (2012) 063415 [arXiv:1206.1875].

[32] M. Gu, *The flexible atomic code*, *Canad. J. Phys.* **86** (2008) 675.

[33] A. Thompson et al., *X-ray Data Booklet*, Lawrence Berkeley Laboratory, (2001).

[34] R.S. Mulliken, *Potential Curves of Diatomic Rare-Gas Molecules and Their Ions, with Particular Reference to Xe_2*, *J. Chem. Phys.* **52** (1970) 5170.

[35] A. Hitachi, T. Doke and A. Mozumder, *Luminescence quenching in liquid argon under charged-particle impact: Relative scintillation yield at different linear energy transfers*, *Phys. Rev.* **B 46** (1992) 11463 [INSPIRE].

[36] E. Aprile and T. Doke, *Liquid Xenon Detectors for Particle Physics and Astrophysics*, *Rev. Mod. Phys.* **82** (2010) 2053 [arXiv:0910.4956] [INSPIRE].

[37] C.E. Dahl, *The physics of background discrimination in liquid Xenon, and first results from Xenon10 in the hunt for WIMP dark matter*, Ph.D. Thesis, Princeton University (2009) [INSPIRE].

[38] J. Lindhard, V Nielsen, M. Scharff and P.V. Thomsen, *Integral equations governing radiation effects*, *Mat. Fys. Medd. Dan. Vid. Selsk.* **33** (1963).

[39] A. Hitachi, *Properties of liquid xenon scintillation for dark matter searches*, *Astropart. Phys.* **24** (2005) 247 [INSPIRE].

[40] P. Sorensen and C.E. Dahl, *Nuclear recoil energy scale in liquid xenon with application to the direct detection of dark matter*, *Phys. Rev.* **D 83** (2011) 063501 [arXiv:1101.6080] [INSPIRE].

[41] P. Sorensen, *Atomic limits in the search for galactic dark matter*, *Phys. Rev.* **D 91** (2015) 083509 [arXiv:1412.3028] [INSPIRE].

JHEP03(2018)194

[42] P. Sorensen et al., *Lowering the low-energy threshold of xenon detectors*, PoS(IDM2010)017 [arXiv:1011.6439] [INSPIRE].

[43] M. Horn et al., *Nuclear recoil scintillation and ionisation yields in liquid xenon from ZEPLIN-III data*, *Phys. Lett.* **B 705** (2011) 471 [arXiv:1106.0694] [INSPIRE].

[44] XENON100 collaboration, E. Aprile et al., *Response of the XENON100 Dark Matter Detector to Nuclear Recoils*, *Phys. Rev.* **D 88** (2013) 012006 [arXiv:1304.1427] [INSPIRE].

[45] LUX collaboration, D.S. Akerib et al., *Low-energy* (0.7–74 *keV*) *nuclear recoil calibration of the LUX dark matter experiment using D-D neutron scattering kinematics*, arXiv:1608.05381 [INSPIRE].

[46] E. Aprile et al., *Scintillation response of liquid xenon to low energy nuclear recoils*, *Phys. Rev.* **D 72** (2005) 072006 [astro-ph/0503621] [INSPIRE].

[47] A. Manzur, A. Curioni, L. Kastens, D.N. McKinsey, K. Ni and T. Wongjirad, *Scintillation efficiency and ionization yield of liquid xenon for mono-energetic nuclear recoils down to* 4 *keV*, *Phys. Rev.* **C 81** (2010) 025808 [arXiv:0909.1063] [INSPIRE].

[48] K. Abe et al., *XMASS detector*, *Nucl. Instrum. Meth.* **A 716** (2013) 78 [arXiv:1301.2815] [INSPIRE].

[49] D. Tucker-Smith and N. Weiner, *Inelastic dark matter*, *Phys. Rev.* **D 64** (2001) 043502 [hep-ph/0101138] [INSPIRE].

[50] R. Essig, A. Manalaysay, J. Mardon, P. Sorensen and T. Volansky, *First Direct Detection Limits on sub-GeV Dark Matter from XENON10*, *Phys. Rev. Lett.* **109** (2012) 021301 [arXiv:1206.2644] [INSPIRE].

[51] R. Essig, T. Volansky and T.-T. Yu, *New Constraints and Prospects for sub-GeV Dark Matter Scattering off Electrons in Xenon*, *Phys. Rev.* **D 96** (2017) 043017 [arXiv:1703.00910] [INSPIRE].

[52] T. Takahashi et al., *Average energy expended per ion pair in liquid xenon*, *Phys. Rev.* **A 12** (1975) 1771 [INSPIRE].

[53] C. Kouvaris and J. Pradler, *Probing sub-GeV Dark Matter with conventional detectors*, *Phys. Rev. Lett.* **118** (2017) 031803 [arXiv:1607.01789] [INSPIRE].

[54] C. McCabe, *New constraints and discovery potential of sub-GeV dark matter with xenon detectors*, *Phys. Rev.* **D 96** (2017) 043010 [arXiv:1702.04730] [INSPIRE].

[55] D.Z. Freedman, *Coherent neutrino nucleus scattering as a probe of the weak neutral current*, *Phys. Rev.* **D 9** (1974) 1389 [INSPIRE].

[56] D.Z. Freedman, D.N. Schramm and D.L. Tubbs, *The Weak Neutral Current and its Effects in Stellar Collapse*, *Ann. Rev. Nucl. Part. Sci.* **27** (1977) 167.

[57] A. Drukier and L. Stodolsky, *Principles and Applications of a Neutral Current Detector for Neutrino Physics and Astronomy*, *Phys. Rev.* **D 30** (1984) 2295 [INSPIRE].

[58] A. Serenelli, *Alive and well: a short review about standard solar models*, *Eur. Phys. J.* **A 52** (2016) 78 [arXiv:1601.07179] [INSPIRE].

[59] R. Essig, J. Mardon and T. Volansky, *Direct Detection of Sub-GeV Dark Matter*, *Phys. Rev.* **D 85** (2012) 076007 [arXiv:1108.5383] [INSPIRE].

[60] P.W. Graham, D.E. Kaplan, S. Rajendran and M.T. Walters, *Semiconductor Probes of Light Dark Matter*, *Phys. Dark Univ.* **1** (2012) 32 [arXiv:1203.2531] [INSPIRE].

JHEP03(2018)194

[61] Y. Hochberg, Y. Zhao and K.M. Zurek, *Superconducting Detectors for Superlight Dark Matter*, *Phys. Rev. Lett.* **116** (2016) 011301 [arXiv:1504.07237] [INSPIRE].

[62] S.K. Lee, M. Lisanti, S. Mishra-Sharma and B.R. Safdi, *Modulation Effects in Dark Matter-Electron Scattering Experiments*, *Phys. Rev.* **D 92** (2015) 083517 [arXiv:1508.07361] [INSPIRE].

[63] R. Essig, M. Fernandez-Serra, J. Mardon, A. Soto, T. Volansky and T.-T. Yu, *Direct Detection of sub-GeV Dark Matter with Semiconductor Targets*, *JHEP* **05** (2016) 046 [arXiv:1509.01598] [INSPIRE].

[64] Y. Hochberg, M. Pyle, Y. Zhao and K.M. Zurek, *Detecting Superlight Dark Matter with Fermi-Degenerate Materials*, *JHEP* **08** (2016) 057 [arXiv:1512.04533] [INSPIRE].

[65] Y. Hochberg, Y. Kahn, M. Lisanti, C.G. Tully and K.M. Zurek, *Directional detection of dark matter with two-dimensional targets*, *Phys. Lett.* **B 772** (2017) 239 [arXiv:1606.08849] [INSPIRE].

[66] F. Kadribasic, N. Mirabolfathi, K. Nordlund, E. Holmström and F. Djurabekova, *Directional Sensitivity In Light-Mass Dark Matter Searches With Single-Electron Resolution Ionization Detectors*, arXiv:1703.05371 [INSPIRE].

[67] G. Cavoto, F. Luchetta and A.D. Polosa, *Sub-GeV Dark Matter Detection with Electron Recoils in Carbon Nanotubes*, *Phys. Lett.* **B 776** (2018) 338 [arXiv:1706.02487] [INSPIRE].

[68] W. Kohn and L.J. Sham, *Self-Consistent Equations Including Exchange and Correlation Effects*, *Phys. Rev.* **140** (1965) A1133 [INSPIRE].

[69] D.H. Sampson, H.L. Zhang, A.K. Mohanty and R.E.H. Clark, *A Dirac-Fock-Slater approach to atomic structure for highly charged ions*, *Phys. Rev. A* **40** (1989) 604.

JHEP03(2018)194